Morphometric Analysis of Granular Impact Craters through Time-of-Flight Cameras

Depth Prediction Model and Lateral Opening Mechanisms

M.Sc. Frank Corrales Machín

Advisor: Dr. Yuri Nahmad Molinari

Institutional Doctorate in Engineering and Materials Science (DICIM)
Autonomous University of San Luis Potosí

This dissertation is submitted for the degree of
Doctor in Engineering and Materials Science

May 2024

"Dedicated to my beloved daughters Bianca and Galicia, perpetual sources of my inspiration . . . "

Acknowledgements

I would like to express my sincere gratitude to Dr. Yuri Nahmad Molinari, Dr. Roberto Bartali, and Dr. Ernesto Altshuler for their invaluable assistance in preparing this thesis. Additionally, I would like to thank the staff of the Institutional Doctorate in Engineering and Materials Science (DICIM) program and the Institute of Physics for their support. F. Corrales-Machin acknowledges the CONAHCYT scholarship with CVU 1050049.

I extend my heartfelt gratitude to Stephania, my life companion, for being my strength and support in every step we take as a family. Your unconditional love sustains me. To my daughters, sources of joy and inspiration in my life, I offer my deepest thanks. To my parents, for instilling in me the drive to succeed, believing in me, and always providing that extra push that has enabled me to persevere. Thank you for dedicating your lives to our family. To my second parents, Doñita Luche and Don Rubén, for embracing me as a son and showering us with love. This thesis is also dedicated to you. To my brother, for always standing by my side, upholding the belief that family comes first, and that it should always remain united regardless of distance. Gratitude extends to the rest of the family in Xalapa for the abundant joy and laughter-filled moments. I cannot overlook the invaluable support of my friends during this phase of my life. What would I have been without the nights of venting and camaraderie in our COD&DOTA group? Our conversations about life, laughter, and good-natured banter against opponents were truly uplifting. Special thanks to Les Papichinēs for welcoming me into their lives; you are indeed family. I am particularly grateful to Alejandro Zepeda for his unwavering support throughout this journey.

Finally, I want to express my gratitude to Andrés, Leandro, and Laciel. More than friends, you have been brothers for many years. Thank you for always being there.

Abstract

Laboratory made granular-granular impact craters have been used as model analogues of planetary impact craters. These kind of craters have been observed and studied using profilometry techniques that allow to retrieve important morphologic features from the impacted surface. In this thesis, we propose to use a Time-of-Flight camera (Microsoft Kinect One) for the acquisition of depth data. We show comparisons between the typically used technique and the analysis derived from the Time-of-Flight data. We also release *craterslab*, a Python library developed to automate most of the tasks from the process of studying impact craters produced by granular projectiles hitting on the surface of granular targets. The library is able to acquire, identify, and measure morphological features of impacted surfaces through the reconstruction of 3D topographic maps. Our results show that using a Time-of-Flight camera and automating the data processing with a software library for the systematic study of impact craters can produce very accurate results while reducing the time spent on different stages of the process.

This study investigates granular impact craters on both loosely and more tightly packed sand targets. We observe significant deviations in the depth vs. energy power-law predicted by previous models. To address this discrepancy, we introduce a physical model of uniaxial compression that explains how depth saturates in granular collisions.

Furthermore, our results reveal a greater transfer of vertical to horizontal momentum on compacted surfaces compared to loosely packed sandbox targets, and we present an energy balance that describes it.

Central peak formation also appears to play an essential role in better transferring vertical momentum to horizontal degrees of freedom, resulting in shallow craters on compacted sandbox targets. However, this is an open topic for further investigation.

On the other hand, we report granular vs. granular experiments that consistently adhere to power-law scaling laws for diameter as a function of impacting energy, similar to those reported by other groups for their experiments utilizing both solid and granular projectiles. However, this result deviates significantly on compacted impact surfaces. To address this, we developed a radial model of lateral opening mechanism where a logarithmic dependence of the diameter on energy is obtained. This is experimentally confirmed.

Our findings indicate that the depth-to-diameter aspect ratio results are consistent with prior and novel observational data from planetary bodies, providing significant insights into the physical processes governing natural crater formation and allowing us to interpret the shallowness of planetary craters in light of the uniaxial compression mechanism proposed in this work. Finally, counterintuitively, we found that the rim height abruptly saturates concerning the impact energy, creating a new paradox for the scientific community.

Table of contents

List of figures

Chapter 1

Crater Formation: A Theoretical Framework

1.1   From Galileo to the present

In 1609, Galileo achieved the first observation of lunar craters. His observations were subsequently confirmed by colleagues, gaining support within the scientific community of the time. In 1610, he published "The Starry Messenger" (Sidereus Nuncius), featuring an illustrative sketch of the Moon and its remarkable elevations (see Figure 1.1). At that time, Galileo had no clues about the origin of lunar craters, and their formation remained an astrophysical puzzle for more than three centuries.

Fig. 1.1 Galileo's sketch of the Moon.
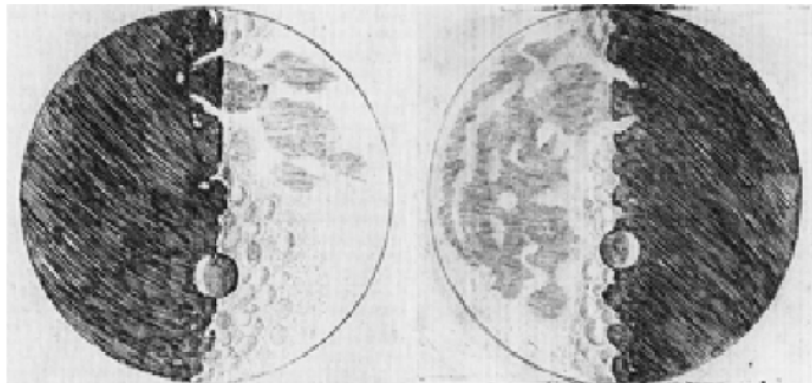
During this period, volcanic activity was initially attributed as the likely cause [44]. While there were some indications that led to the hypothesis of formation due to collisions with astronomical objects, it was largely dismissed at the time, considering interplanetary space as a void.It was not until the discovery of asteroids that the concept of collisions was revisited. In

1892, Grove Gilbert presented his theory of crater formation, which was linked to Laplace's protoplanetary cloud model of solar system formation [37]. Later, in 1921, Alfred Wegener proposed the hypothesis of a meteoritic origin based on impacts involving speeds greater than the lunar escape velocity [118]. In the 1960s, geologists and astrophysicists began to embrace this idea [103], and it has persisted to the present day.

Asteroids are considered the remnants of the solar system, representing material that never coalesced to form planets. The first asteroid was discovered in 1801 by Giuseppe Piazzi, marking the beginning of an endless list of discoveries, including Pallas, Vesta, Hygiea, Davida, Interamnia, and more. Currently, there are at least two million unnamed asteroids in the Solar System, with the majority located in the main asteroid belt between the orbits of Mars and Jupiter.

Planetary scientists widely agree that a significant number of craters in the Solar System were formed approximately 4.6 to 4 billion years ago during the era of intense meteoritic bombardment. Undoubtedly, craters serve as the scars of the solar system, and through their study and classification, valuable insights into the origin of the solar system can be obtained.

1.2   Crater Classification

Planetary surfaces reveal the remnants of cataclysmic events that have left traces observable millions of years later. Mars has $384,343$ craters with diameters $\geq 1\,\text{km}$ [92], and the Moon has approximately the same number. We encounter an endless number of craters, both large and small, on the planetary surfaces of the Solar System.

Although all craters share some similarities (being surface indentations with well-defined depths and diameters), they exhibit variations in certain details. It is these details that are crucial for constructing a comprehensive morphology [6]. Given the wide range of crater sizes, from a few meters to others spanning diameters from $50\,\text{km}$ to $700\,\text{km}$, a classification becomes imperative. This is particularly evident as the size inherently shapes their forms.

Craters can be classified into two groups: simple and complex craters. Examples from both types can be inspected in Figures 1.2a and 1.2b, respectively (for multiple examples, refer to [96]).

Simple craters are bowl-shaped depressions with raised rims and approximately parabolic interior profiles. A straightforward structure that presents a circular or elliptical rim with the rim-to-floor depths of a large sample of simple craters on the moon are roughly $1:5$ of the rim-to-rim diameter.

Complex craters possess a variety of features and a more complicated structure than simple craters. They often exhibit a central structure in their interior (central peak or dome)

which may protrude above the crater rim. Images from Lunar Reconnaissance Orbiter Camera (LROC) shows craters with single or multiple central peaks, concentric rims and flat inner floors. The depths of complex craters increase with increasing diameter, but they increase much more slowly than the depths of simple craters.
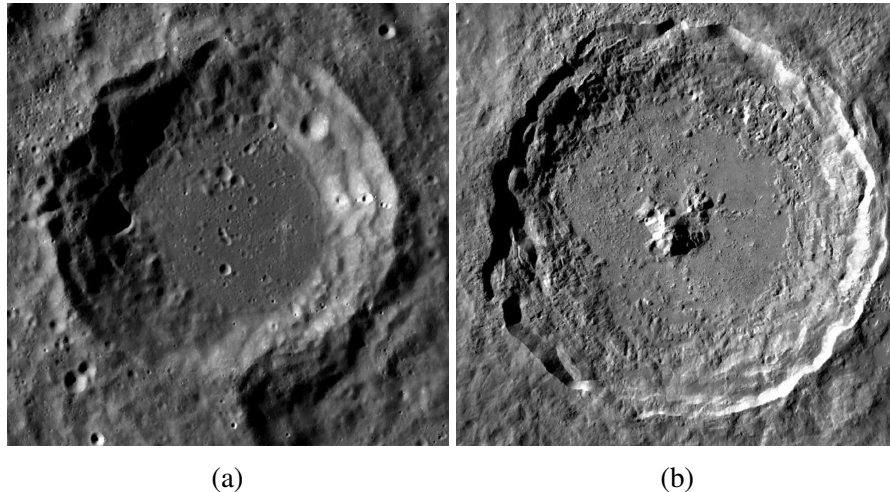
Fig. 1.2 Crater classification. (a) Simple crater Steinheil (b) Complex crater Tycho. Images taken from [62, 59].

In the presence of these different morphologies, some questions have arisen in the planetary science community: *"What intricate and highly non-linear processes led to the formation of such landscapes? What type of projectile struck the Moon, giving rise to the Tycho crater [18] (Figure 1.2b)? What were its kinetic energy, size, and density? If we ever prove the hypothesis that the extinction of dinosaurs resulted from the violent collision of a large meteoroid on the coast of Mexico, what details surround such a Cretaceous-Tertiary extinction event? Considering the higher probability of oblique impacts, why do the majority of craters in the Solar System exhibit a circular shape?"* These are among the questions scientists have attempted to answer [96].

1.3   Theoretical Frameworks

The scientific community, in its attempt to answer these questions, has sought to reproduce these catastrophic planetary events. However, how can one achieve such a reproduction? Considering that meteorite impacts trigger catastrophic events such as shock melting and evaporation, processes that are impossible to replicate in a laboratory, the tool to use is numerical simulations. By providing the correct equations and properties of the impactor and the target, multiple simulations can be conducted, yielding various results.

Currently, these codes have reached a level of sophistication where a web-based computer program exists with the specific purpose of predicting the catastrophic consequences of a meteor impact on our planet [21]. These numerical models, known as hydrocodes [84], stand as the benchmark in planetary science. However, despite their advanced capabilities, scientists emphasize the need for caution in their application, as these codes, on their own, lack the capability to determine which physics is essential to consider [42]. Significant challenges still persist, such as effectively addressing porous bodies [120, 26, 11].

In this context, a theoretical framework was formulated that involves hypervelocity impacts, always greater than the lunar escape velocity, where the colliding objects are solid bodies. Currently, there exists a well-established understanding of the processes involved in impact crater formation, which has been derived from geophysical exploration of terrestrial impact craters, computer simulations (hydrocodes), and hypervelocity experiments. These processes can be categorized into three main stages: contact and compression, excavation of a transient crater, and modification through avalanching and deposition of debris [72, 79]. However, due to their rare occurrence and the immense energy involved, impacts that form planetary craters are infrequent events that are difficult to observe directly. Consequently, it is challenging to gather experimental or observational evidence to directly compare and validate the theoretical understanding of impact crater formation.

On the other hand, reproducing crater formation in a laboratory may seem impossible. However, we could consider the following: we are dealing with massive bodies (asteroids) impacting the surface of planets at hypervelocities. Would it be possible to revive these events in a laboratory by reducing the size from kilometers to centimeters and impact velocities from kilometers per second to meters per second? The theory of scaling [13] might provide a path to finding the essence of this complex phenomenon. The goal is to reduce the complexity of a given dynamics, where a large number of degrees of freedom interact with each other in an unknown way, to find a more economical picture where a few variables relate through simple scaling relations. If carefully carried out, scaling provides a framework that unifies data taken under dissimilar conditions. This idea planted the seed in several scientists, prompting them to try to reproduce crater formation at the laboratory level [4, 5, 115, 51, 110]; thus attempting to build a bridge between planetary impact-cratering events and similar events restricted to a laboratory bench.

Using proportionality laws or scaled systems, the Scottish geologist and geographer Henry Cadell played a pivotal role in advancing the field of analog model studies through sandbox experiments. His work focused on investigating the formation of thrust and fold systems in the Scottish Highlands. Subsequently, scaled analogue modeling has become a commonly employed technique for studying the geometric, kinematic, and dynamic evolution

of various geological structures. This powerful tool allows for a comprehensive understanding of the geometric and kinematic development of extensional, inverted fault systems, as well as strike-slip fault systems.

The remarkable resemblance between the scaled models and the natural geological examples described in the literature highlights the effectiveness of this method in accurately replicating real-world geological structures [69]. However, this technique has been, just very recently, incorporated for understanding Impact craters as geologic processes [9] by considering equal adimensional numbers (e.g. Reynolds and comminution numbers), regardless of the fact that man made laboratory craters and observed planetary craters are produced by events differing in six or more orders of magnitude [38, 82].

1.3.1 Granular Collisions and the Formation of Solar System Bodies: A New Perspective

The nebular model proposed by Marquis de Laplace [119] for the formation of the Solar System involves the accretion of a dust interstellar cloud, forming a disk that orbits around a center originating from a density fluctuation in the original cloud that spontaneously breaks the translational symmetry of it. During the accretion process, local density fluctuations in the newly formed accretion disk give rise to new centers of attraction and the consequent formation of granulated asteroids, planetesimals, and eventually the formation of dwarf planets, planets, giant planets, or the formation of binary star systems if the mass of a pair of these attracting centers exceeds the critical mass to initiate thermonuclear fusion reactions.

During the aforementioned accretion process, the primary dominant attractive force is the van der Waals force or London dispersion forces [101]. This is due to the induction of an electric dipole in a dust mote by the appearance of an electric dipole in a neighboring particle, caused by a fluctuation in the surrounding electromagnetic field. Due to the small size of the dust particles in the primordial cloud, gravitational forces between them will be minuscule compared to the van der Waals forces. Despite decreasing inversely proportional to the sixth power of the distance between particles, electrostatic forces turn out to be orders of magnitude higher in intensity than the corresponding gravitational attractions between both dust grains.

It can then be assumed that the formation of asteroids, planetesimals, and other smaller bodies in the solar system, such as comets, is an inherently granular process. In other words, it is a process involving many bodies that interact dissipatively through Coulomb friction and partially inelastic collisions.

It is interesting to review the image that has been formed of collisions between celestial bodies, portraying them as cataclysmic events where an iron meteorite projectile several kilometers in diameter impacts Earth, resulting in events such as the extinction of dinosaurs. It is then worth asking why the surfaces of Earth and the Moon appear so dissimilar. Can the limited number of craters on Earth be explained solely by erosion caused by geological flows? How does the loosely consolidated nature of comets and asteroids influence impact crater formation processes?

The relative velocity and, consequently, the collision energy between two objects —the larger one referred to as the target and the smaller one as the bolide or projectile— depend on the causes of the relative motion between these objects. Considering objects in an accretion disk orbiting around a forming star, the relative velocity between a forming planet and an asteroid could be determined solely by the escape velocity of the planet or planetesimal. On the other hand, if the collision is the result of the fortuitous intersection between a planet and a comet (highly dissimilar, uncorrelated orbits), then the relative collision velocity will be a fraction of the escape velocity of the central star in the accretion disk.

In the case of the formation of planetesimals, comets, and minor bodies, collisions will be of low energy with velocities on the order of meters to tens of meters per second. On the other hand, for planets, dwarf planets, and moons, collisions involve velocities on the order of kilometers to tens of kilometers per second (hypervelocity).

It can be said that the minor bodies of the solar system are a stack of rubble [122, 113] grouped only by very weak forces, making them very fragile or weakly consolidated objects [120, 56, 46]. This image has been confirmed with the direct observation of asteroids Eros and Itokawa, visited by space probes that sent high-resolution photographs of these objects, confirming their granular nature or "rubble pile" [80]. As the size of the analyzed bodies increases, and following the equation of hydrostatic equilibrium, the pressure in the core of a planetesimal increases with its size, reaching values where metamorphic processes begin, depending in part on the abundance of radioactive elements heating that planetary core. These metamorphic processes, together with diagenetic or lithification processes by cementation and chemical reactions of accreted materials, modify the hardness of the planetesimal. As its size and complexity increase, it gradually becomes a more consolidated body with greater cohesion [88, 116].

Considering collisions where the collision energy exceeds the cohesion energy of the bodies implies that the collision will be disruptive, dispersing the material instead of promoting accretion and planetesimal growth (as in the case of Ultima Thule, officially named 2014MU69). Similarly, collisions that, due to the impact parameter, are very grazing or oblique, will also not encourage the aggregation of the two bodies. Hence, it is important to

study low-energy collisions between weakly consolidated bodies that collide guided by their gravity in a normal way. These conditions should be the most abundant in the early stages of planetary formation and likely mark the surfaces of minor bodies in all planetary systems today.

Up to now, projectiles have been regarded as solid bodies in the granular physics and planetary science communities, and it is considered that at hypervelocities (using hydrocodes), a granular projectile also melts or evaporates [84]. However, does the course of events originally proposed by Melosh—contact and compression, cavity growth and collapse—still hold if the impacting projectile is also granular and undergoes comminution or crumbling instead of melting and evaporation? If asteroids are not consolidated bodies but aggregates (although not necessarily gravitational), how does this fact modify the current paradigm of crater formation?

In this context, although the origin of craters in planetary bodies of the Solar System is no longer an astrophysical puzzle [85, 118, 93] and the root of their morphology seems to be a settled issue [72, 71, 43], the evidence that increasingly builds up on the granularity of asteroids [46, 8, 34, 101] hints toward a critical revision of the existing paradigm which fails to explain certain features like the existence of boulders perched on central peaks. This paradigm states that craters and central peaks were created by the target fluidization produced by solid meteorite impacts, followed by the collapse of the transient crater where the final shapes of craters emerge.

Therefore, it is crucial to expand our understanding of the dynamics of low-velocity crater formation between objects of a fragile nature, such as the aggregates of dust, rocks, and ice that make up asteroids, comets, and other minor bodies in the solar system.

1.4   Space Observations

Since the Apollo missions, spacecraft have been instrumental in capturing images of planets, moons, and asteroids within the Solar System for investigative purposes. Scientists have provided detailed descriptions of these celestial bodies utilizing various optical methods, including shadow measurements [86], photoclinometry [49, 30], stereo image analysis [36], or a combination of these techniques [12]. While many morphometric features are necessary for their comprehensive description, the primary dimensions used are diameter and depth. Some ambiguities arise concerning how to precisely define these two measures, as discussed, for example, in [108]. Nowadays, reliable sources exist where millions of craters are classified.

One of the primary online platforms for accessing this data is Applied Coherent Technology (ACT) Corporation, where multiple layers of information can be accessed, and its primary objective is to make fundamental scientific discoveries about the Moon, Mars, and Mercury. *"Founded in* 1988*, has emerged as one of the highly innovative and trusted organizations in the geospatial data applications industry. ACT was founded by Dr. Erick Malaret. Dr. Malaret holds a PhD from Purdue University in Electrical Engineering with a specialty in Signal/Image Processing and has over* 35 *years of experience in the field. Dr. Malaret has devoted his career to developing software that enhances the efficiency and quality of the image data analysis process - beginning with his doctoral research in remote sensing and image systems in the* 1980*s. Dr. Malaret has focused his efforts and ACT's research and development resources across the complete image data analysis lifecycle - from sensor data capture and management through analysis and end user results. This unique approach has produced groundbreaking software for managing the entire process, improving research results and enabling significant reuse of data and research findings."* [32]. This data acquisition system operates with Light Detection and Ranging (LiDAR) technology.

The crater database in our Solar System is continually expanding, providing easy access to high-precision morphometric features. This facilitates the possibility of making comparisons between laboratory experiments and observational data. However, it is crucial to understand the measurement techniques applied in terrestrial experiments to simulate crater formation. Are they precise enough to establish a correct relationship when compared to observational data? Do they cover all the necessary morphology for a precise analysis? Let's examine this further.

1.5   Mapping of surfaces

Determining unknown distances to objects or their spatial dimensions by measuring the angles they form from known points of observation is an ancient technique known as triangulation, which is still used in modern instruments. In the sixth century BC, Thales of Miletus measured the height of pyramids by comparing the ratio of their shadow length to height with his own shadow length to height ratio at the same time, using the Thales theorem of corresponding proportions. Shortly after, Eratosthenes measured the radius of the Earth, while Aristarchus of Samos calculated the sizes of the Sun and Moon, as well as their distances from the Earth in Earth radii, based on the same geometric principles. This led to the development of a heliocentric model of our solar system, utilizing a simple yet powerful set of geometric theorems, thousands of years ago [48].

The importance of meteorite impacts for Earth and life on Earth evolution was recognized in 1980, when the Chicxulub crater in the Yucatán peninsula was recognized as the scar of a colossal impact that caused the mass extinction event at the Cretaceous - Paleogene (K-Pg) boundary 65 Ma ago [1, 2]. Initially, projected shadow length was used to determine the depth of craters and the height of their rims in early studies of lunar geophysical features [17]. Subsequently, satellite radar altimetry using real-time of flight techniques [25] was employed to explore topographic features and create elevation maps. Eventually, phase-change Time-of-Flight techniques, such as LiDAR, were introduced for atmospheric, terrestrial, and planetary science prospecting.

In order to investigate the influence of impact collision energy on the final shape of craters, various techniques have been employed for the characterization of morphological features of craters such as laser profilometry or direct measurements [27]. These techniques provide valuable insights into the characteristics and behavior of impact craters, aiding in the understanding of the relationship between the energy involved in the event and the resulting crater morphology and sedimentologic features.

Three-dimensional measurement and reconstruction of surfaces is a significant topic in various fields of research, with diverse applications such as range scanning [124], industrial inspection of manufactured parts [39], reverse engineering (digitization of complex, free-form surfaces) [57, 14], object recognition and 3D mapping [104, 94]. Currently, several techniques are implemented for these measurements, benefiting from significant technological advancements that enable high resolutions and software with multiple domain-specific features. However, access to these software often comes with a high financial cost.

In the context of mapping granular-type impact craters, the scientific community primarily relies on profilometry as the preferred technique for obtaining morphological characteristics. However, the idea of implementing depth measurement techniques based on range sensors, such as LiDAR, in this field of research is highly appealing. In this section, we will explain the operating principle of both techniques and their general limitations, with a deeper focus on their application for the study of craters morphology.

1.5.1   Profilometry-based Methods

With the current technological advances in acquiring three-dimensional surface maps, different profilometry techniques have been refined to obtain more reliable results in shorter time [111, 97, 105]. Despite these advancements, most of these techniques are challenging to implement and have limitations such as complex image analysis.

As mentioned earlier, laser profilometry is commonly used to obtain morphological characteristics of craters. This method is based on the principle of triangulation, where a

laser projects a beam of light onto the surface of interest, and a sensor records the position and angle of the reflected beam. With this information, the distance between the sensor and the surface can be calculated, allowing for the reconstruction of a three-dimensional profile.

In addition to laser profilometry, another technique used for measuring depths on crater surfaces is structured light profilometry [35]. In this method, a pattern of structured light, such as stripes or lines, is projected onto the surface, and an image of the illuminated surface is captured. Analyzing the deformations of the light pattern in the image allows for the calculation of local depths of the surface. Structured light profilometry is based on the principle of interferometry, where variations in the surface shape cause changes in the phase and intensity of the reflected light. These changes are captured by a camera and processed to obtain a depth map of the crater's surface.

While laser profilometry and structured light profilometry are widely used techniques for obtaining data for the morphological characterization of granular impact surfaces, they also have certain limitations that are important to consider:

Both laser profilometry and structured light profilometry methods have limitations in resolution due to factors such as sensor-to-surface distance, pixel size, and laser precision. These limitations can impede capturing fine surface details, especially in areas with small features. Additionally, accurately measuring transparent or translucent surfaces can be challenging as light may pass through or be absorbed instead of being reflected, resulting in inconsistent measurements. Reflective surfaces can also pose difficulties, as intense reflections can interfere with measurements and generate inaccurate data. Shadows and obstructed areas on the surface can hinder data capture by causing variations in reflected light intensity or blocking the light pattern projection. Furthermore, measurements obtained through these methods are susceptible to noise and artifacts, which can introduce errors or distortions in the data. These artifacts can arise from fluctuations in light intensity, environmental interference, or device calibration issues. Finally, data acquisition time can be a limitation, particularly when high resolution or sampling large areas efficiently is required, impacting situations that demand fast response times.

In summary, laser profilometry and structured light profilometry are valuable techniques for measuring depths and obtaining three-dimensional surface information. While they have seen improvements in recent years, they still have limitations in terms of implementation complexity and specific challenges related to image analysis. These techniques, nevertheless, offer valuable insights into the morphology of granular impact craters and contribute to the understanding of physical phenomena.

1.5.2   Methods based on LiDAR Sensors

In the last decade, new affordable range detection devices have been developed. Light Detection and Ranging (LiDAR), since the 1960s with the advent of lasers, has emerged as a pioneer in this field, empowering multiple applications [28, 87]. LiDAR technology is based on the Time-of-Flight principle. It measures the time it takes for light emitted by a device to travel to the surface of an object and return to the sensor of the unit. The precise measurement of the time it takes for light to travel and return to the sensor array of a measuring device is determined by the switching velocity of the sensor's microelectronics. Time-of-Flight cameras employ a continuous wave intensity modulation approach, where the surface of interest is illuminated with near-infrared intensity-modulated periodic light. Considering the finite speed of light (c) and the distance between the camera and the surface (assuming the sensor and illumination are in the same location), an optical signal experiences a temporal shift $\phi[d]$, which corresponds to a phase shift in the periodic signal. The phase shift is calculated by considering the charge accumulated in the sensor due to the reflected light when the synchronous shutter turns off the light sampling. By transforming the temporal shift into the sensor-object distance, we obtain the equation $d = 4c\phi\pi$. It is important to note that intermittent illumination of the scene at several gigahertz and rapid switching speeds are crucial for achieving high depth resolution.

Among the various LiDAR devices based on the Time-of-Flight principle, the second generation of Microsoft Kinect (KinectToF) stands out. It offers several improvements over its predecessor, which utilizes structured light (SL) method for depth information acquisition. In the first generation of Kinect, the structured light method involves projecting a sequence of known patterns onto an object, which deform based on the object's shape. The deformed patterns are then captured by a camera, and by analyzing the distortion using triangulation, depth information is derived. Although the Kinect sensor was originally intended for natural user interaction in body-based video games, the release of its source code by Microsoft has led to the development of numerous applications in robotics [31], 3D reconstruction [52, 76, 77], medicine [75], augmented reality and interaction [112], geophysics [91, 106], among others.

Both SL and ToF principles for range detection are susceptible to various sources of error. Several studies have compared these methods and explored different calibration techniques for the Kinect camera [98, 117, 83, 121, 54, 33, 125]. Considering the benefits and limitations of the two different Kinect principles of operation, it has been determined that the second generation, utilizing ToF technology, is superior [50].

To our knowledge, ToF sensors have not yet been used for the study of morphological signatures of experimental impact craters in laboratory. In the study of craters, the LiDAR

system has been employed to automatically measure grain size distribution across a range from pebbles to blocks in outcrops within the Joya Honda crater in Mexico [19]. However, the increasing utilization and affordability of LiDAR and Time-of-Flight instruments for rapid surface topography measurement have prompted us to develop a versatile methodology specifically designed for acquiring and processing topographic data in the study of impact crater formation.

As part of this work, we release a Python library developed to automate our methodology and determine the morphological characteristics of excavated craters in laboratory settings. We expect, that both, our library and our approach on using Time-of-Flight cameras may enable novel studies on granular-granular impact craters serving as model analogues for observed planetary craters.

Chapter 2

Materials and Methods

2.1 Experimental Setup

An experimental system was designed to recreate the formation of impact craters by using, for the first time, a KinectToF sensor for the data acquisition. Considering that laser profilometry is the typically used technique for this purpose, we added it to the experimental setup in order to validate the results obtained by our approach.

We constructed a square-based sandbox with dimensions of 45 cm per side and 15 cm in height as the surface or granular bed in which the crater forms after the impact of a sand lump projectile. Sand grains with a diameter of $d \leq 1.0$ mm, obtained by sieving, were deposited inside the box as the granular medium.

Two equally prepared series of fragile projectiles were launched at different heights, ranging from 0.1 m up to 20 m, in free fall. After conducting 15 dropping experiments from a 20 m height, a final velocity of 18.55 ± 1.23 m/s was measured, demonstrating good reproducibility. This results in a deviation of less than 5.67 % from the theoretically calculated final speed of 19.78 m/s in this worst-case scenario. For smaller dropping heights, the error due to air drag is reduced. They impacted the free surface of a sandbox filled with loose or compacted sand in order to explore the influence of a more consolidated terrain on the crater formation mechanism and the final morphological features of the resulting craters.

The projectiles were prepared by compacting a mixture of wet sand (250 g of sand plus 47.5 ml of water) with 5.0 g of Portland cement (Portland Type II Compound CPC 30R RS, Cemento Cruz Azul) as an adhesive, constituting only 2 % of the total weight. This blend was introduced into a spherical mold. The resulting projectiles are weakly consolidated granular spheres, exhibiting a diameter of 7.07 cm, a mass of 242.51 g, a density of $\rho = 1.31$ g/cm^3, and a packing fraction of $\phi = 0.50$. Subsequently, the projectiles were allowed to dry at room

temperature for one week. Finally, post-drying, their yield strength was measured, denoted by $\sigma = 17.15 \pm 2.2$ kPa.

The sand utilized on the impact surface is the same material from which the granular projectiles were crafted. The density of solid silica is $\rho_g = 2.65$ g/cm^3, and the angle of repose fluctuates between $40°$ and $44°$. Decompaction of the sandbox target was accomplished by uniformly raking the granular medium inside the sandbox. To facilitate compaction, an additional 3.5 kg of sand was added to the sandbox, and a uniform pressure of approximately 1.0 kgf/cm^2 was applied to the surface by a mass of 92 kg placed on top of a cover lid of the sandbox. Consequently, the target attained a density for loosely packed sand, $\rho_L = 1.39$ g/cm^3, while the compacted target reached a density of $\rho_C = 1.52$ g/cm^3.

After each collision event, a topographical map of the resulting crater's surface was obtained using a Time of Flight (ToF) camera (Microsoft Kinect One model: $74Z - 00001$) positioned at a height of 102.7 cm perpendicular and stationary to the impact surface. At this working height, a resolution of 2.8025 mm/px is achieved in the X, Y plane, with ± 1 mm accuracy in the vertical axis. The Kinect camera was calibrated, resulting in a measurement error, for the two-dimensional plane, of ± 0.16 px with respect to the field of view of the infrared camera of 512×424 px. After each collision event two depth maps are acquired; the first one containing all projectile fragments that may be present on the surface, and for the second one, the interfering projectile fragments are removed to facilitate the morphological analysis of the impacted surface.

Subsequently, the morphological characteristics of the formed crater are automatically detected and quantified using the Python library *craterslab*, specifically designed for such purposes and offering morphometric features of experimental and planetary impact craters in an automated way [23]. The quantified features, plotted as functions of the impact energy, encompass parameters such as crater depth, major and minor diameters, central peak height, as well as the volumes of both the crater cavity and the material deposited above the original surface level.

The laser profilometry technique is performed as well in order to compare and discuss the results of both methods. It is conducted without a sensor for automated data acquisition. Instead, a laser beam is used to project five lines onto the granular bed at a 45-degree angle. Scanning is performed at different points on the surface, and images are captured for each position. Subsequently, these images are processed using *ImageJ* software [10], employing the principle of triangulation to obtain depth and diameter measurements of the crater under study. The procedure of using laser profilometry to obtain morphological characteristics is well-known and established in the field.

Next, we will address some definitions related to morphological observables (implemented by *craterslab*) of impact craters.

2.2   Main Crater Observables

According to the crater classification described in Section 1.2, let's define the morphometric measurements (observables) that will enable us to conduct subsequent morphological analyses. We will establish the original ground surface as the zero reference for heights and depths [79]. From this reference point, we will consider the positive Z axis as an increase in height above the surface, and the negative axis as a decrease in surface level.

For both morphologies (simple and complex) depicted in Figure 1.2 there may be deposits of granular material in the interior of the crater, which are remnants of the impacting granular projectile. Therefore, the maximum excavated observable depth d_{exc} may be smaller than the actual crater depth d_t. Both measurements of depth are typically below the original ground surface. The excavated depth is the crater depth commonly used in the scientific community. Meanwhile, in the astronomical community, the crater depth (d_{max}) is defined as the distance between the crater rim height (h_{rim}) and the deepest point inside it (d_{exc}). In any case, we will use both later on.

The height of the central peak H_{cp} can be defined as the difference between its maximum depth value d_{cp} and the maximum excavated observable depth d_{exc}. The Figure 2.1 illustrates a visual representation of these definitions.
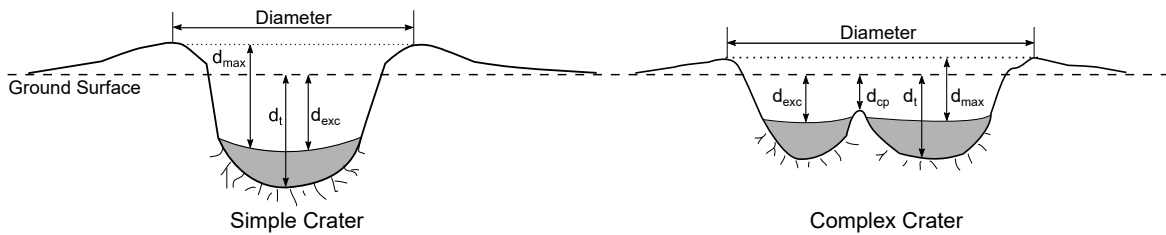
Fig. 2.1 Definition of some observables for simple and complex craters.

From Figure 1.2 we can notice that craters generally have an elliptical geometry, where a circular approximation of their surface is a special case of an ellipse. To determine the type of geometric approximation that best fits their surface, Equation (2.1) can be fitted on samples from the distribution of maximum height values around the crater rim h_{rim}.

Once this ellipse is obtained, the values of *a* and *b* are fixed, which represent the major and minor radii of the ellipse, respectively. In the case of a circular fit, these values will be equal. Additionally, x_c and y_c represent the *x* and *y* coordinates of the center of the ellipse.

Finally, Equation 2.1 fitted over the rim provides the variables θ and $\varepsilon = \dfrac{\sqrt{a^2 - b^2}}{a}$, which are the rotation angle and eccentricity of the ellipse that represents how circular or elliptical the surface of the crater is in function of it diameters.

$$\frac{[(x-x_c)\cos\theta + (y-y_c)\sin\theta]^2}{a^2} + \frac{[(x-x_c)\sin\theta - (y-y_c)\cos\theta]^2}{b^2} = 1 \qquad (2.1)$$

The diameter $D = 2a$ of both simple and complex craters is defined as the distance equal to the major axis of the best fitting ellipse to the rim. Having an elliptical approximation for a crater simplifies the computation of several observables. For example, the crater diameter D can be conveniently expressed as $D = 2a$. Furthermore, by transforming Equation (2.1) into an inequality, it is possible to quickly determine whether an arbitrary coordinate x, y corresponds to the interior of the crater or not. This can be used to speed up some costly computations, such as finding the maximum excavated observable depth d_{exc} or computing the crater concavity's volume V_{in}.

The concavity's volume V_{in} is the volume contained inside the crater limited to the average value of h_{rim}. This volume is equivalent to the amount of water that can be contained within the crater's concavity if it could be filled up to the average rim's height without being spilled out, considering the rim's height to be uniform all around the fitting ellipse.

The excavated volume V_{ex} is the volume of the hollow under the surface reference ground level within the crater rims. This excavated volume only accounts for the amount of material of the target that has been removed or compressed, but not substituted by the projectile material. As the impact energy increases, larger is the excavated volume, and less material from the projectile remains within the crater.

For complex craters with uplifted central structures, such as central peaks or domes, the crater's depression forms an annular trough. The lowest points of this annular depression delineate a ring-shaped valley, marking the beginning of the uplifted central structure. The volume of the central peak (V_{cp}) corresponds to the space enclosed within the inner ring-shaped valley and is determined based on the average depth of this valley.

On the other hand, we define the deposit excess volume V_{exc} as the volume found above the ground surface. This variable is related to the amount of material ejected and expanded (Reynolds dilatancy [7]) or displaced by the shock wave during the impact and includes all material deposited on the surface, including that of the crater rim. It is important to note that in the case of complex craters, the formation of central peaks may protrude above the ground surface zero reference, and that fraction of the volume of the central peak V_{cp} is considered in the calculation of V_{exc}.

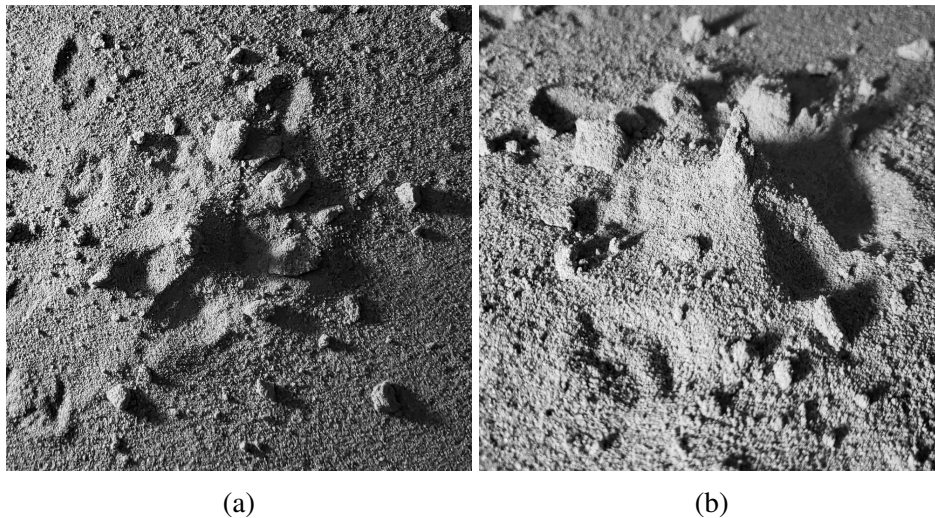(a)   (b)

Fig. 2.2 Impacts at very low energies with no penetration of original ground surface. (a) Perpendicular view respect to the original ground surface (b) Oblique view.

Now, let's delve into a particular case of morphologies observed for impacts with very low energies, where no penetration occurs in the original and compacted ground surface (See Figure 2.2).

These particular morphologies do not meet the definitions of craters, since no depression is formed, and will be considered as sand mounds formed by the remnants of the projectile on the impact surface. These mounds may or may not approximate central peaks. For these cases, only the variables of deposit excess volume V_{exc} and maximum mound height H_m for $z > 0$ values are taken into account.

2.3   Craterslab Software

The study of planetary geology and impact craters encouraged the development of various software tools that aid in the analysis of planetary craters. These software tools provide valuable insights into the formation and evolution of celestial bodies, helping us to better understand the history and structure of our solar system.

Some of the most recent software tools for analyzing planetary craters include craterstats [Michael, Greg and Annex, Andrew and Aye, Michael], CSFD Tools [90], mvtk [70] and PyNAPLE [102]. These software offer a range of features, from 3D visualization and topographic mapping to data analysis and modeling tools. They are widely used by planetary scientists and researchers to study the morphology and history of craters on various celestial bodies.

However, most of the craters-related software have been crafted with a strong focus on planetary craters. While man-made craters have been shown to be useful models for studying the rare events occurred during impact crater formation, specific software tools are required to help process data from these experiments. To address this need, we have developed *craterslab*, a software library that is able to automate data acquisition from Time-of-Flight sensors and process the data to retrieve the main crater morphologic features. The library is open source and packaged for distribution via pypi [Viera López, Gustavo and Corrales Machín, Frank].

It is important to clarify that the library is designed to process data from any depth sensor, although it primarily leverages depth data from the Kinect sensor. However, as part of forthcoming updates we have plans to support other platforms that utilize the time-of-flight (ToF) principle, such as the Femto Bolt from ORBBEC [78]. Therefore, we will extend the tool versatility, encompassing all aspects from depth map acquisition to crater morphological data processing, eliminating the need for integrating external tools.

Our library's functionality extends to various applications, including volcanic crater analysis for the geophysical community, terrestrial impact crater exploration for mining purposes, and integration into the Applied Coherent Technology (ACT) Corporation platform [66] for morphometric analysis of craters in planetary systems like Bennu [24]. By being open source and packaged for distribution via pypi [Viera López, Gustavo and Corrales Machín, Frank], we aim to make the library accessible to a wide range of users.

The software is designed to simplify the data acquisition and analysis process, allowing researchers to focus on the interpretation of results rather than spending time on data processing [22]. It offers a range of features, including automatic data acquisition, real-time data processing, and the ability to visualize and analyze data in a variety of ways. Sample plots produced with *craterslab* can be seen in Figure 2.3.

The workflow of the software can be summarized in: (1) Fetching surface mapping data directly from sensors or locally stored files; (2) Classifying the surface based on the observed formation: simple crater, complex crater or sand mound; (3) Computing the shape of the crater by fitting an ellipse to the crater rim; (4) Determining morphological crater features and (5) Visualizing the results. However, the software is built with flexibility, allowing for independent usage of some of its functionalities.

The different crater's observables computed by the software, described in Section 2.2, allows for various analyses of experimental crater morphology. Variables such as diameter and depth can be more accurately correlated with each other. Others, like cavity volume, can now be determined precisely with numerical integration rather than geometric approximations. For example, it is now possible to calculate the volume of the cavity in the craters represented in Figure 2.4d and Figure 2.4e.

The software is also able to compute the interior slopes of the craters, which allows to determine the incoming direction of the projectile in oblique impacts; the excavated and excess volume, which are related to the amount of material deposited inside the crater, compression and expansion of the terrain, and the ejecta deposited outside the crater after impact. The library automatically detects the crater profile along the diameter, but it also includes the functionality to manually obtain profiles in the desired direction.

Finally, the library includes a pre-trained classification model designed to detect the types of craters present in a depth map. The input to the model is a depth map image with dimensions of 100×100, and the output provides predicted probabilities for different morphologies: Simple Crater, Complex Crater, Sand Mound, or Unknown morphology. The classification model is based on a Convolutional Neural Network (CNN) architecture, comprising two convolutional layers, followed by max pooling layers, a flatten layer, and two dense layers. During the training process, we employed the Adam optimizer with a learning rate of 0.001. The model was trained for 100 epochs on a custom dataset consisting of 400 depth maps containing different morphologies obtained experimentally. Subsequently, we evaluated the model's performance on a separate testing set of 50 depth maps, achieving a classification accuracy of 0.872. It is important to note that our library is not primarily focused on crater classification. Therefore, we acknowledge that there may be more performing approaches that users can explore through *craterslab* for this task, including the utilization of their own models or fine-tuned weights for the provided architecture.

In the following section 2.4, we will illustrate the usage of the software by processing the data obtained following the procedure described in section 2.1.
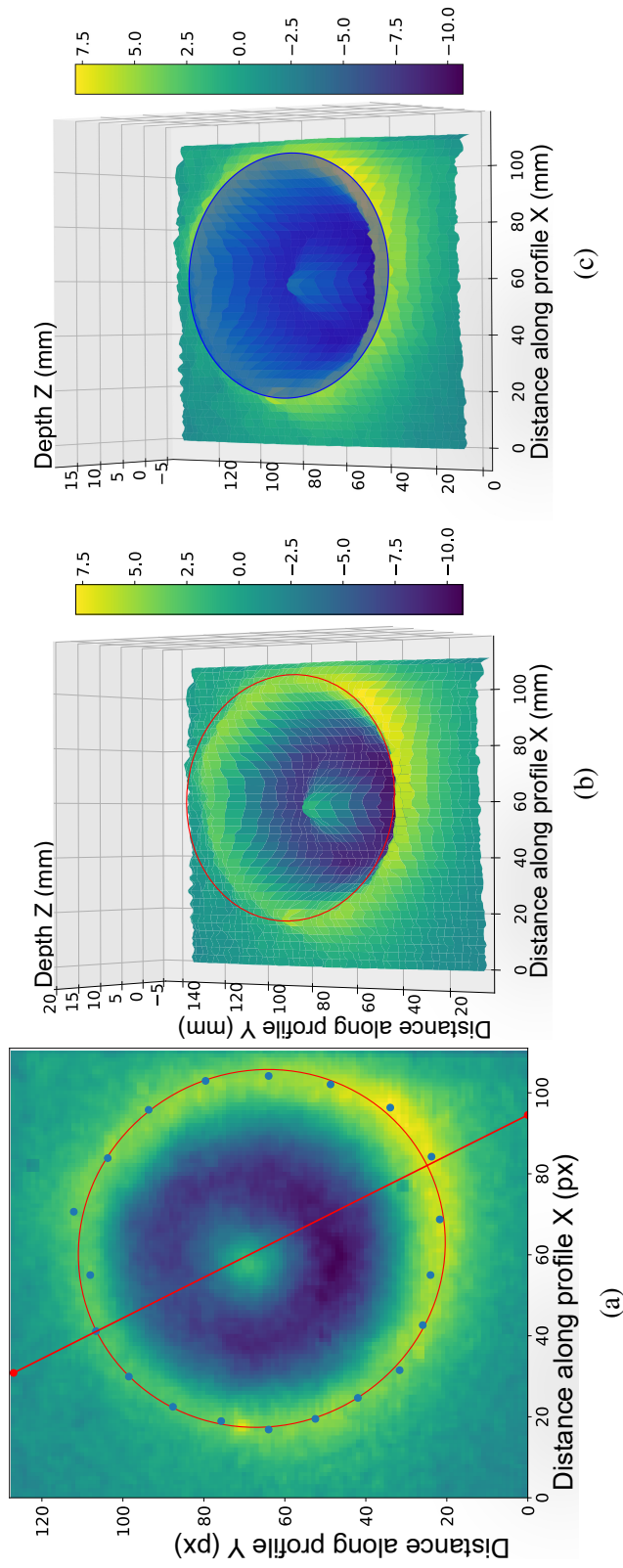
Fig. 2.3 Visualization of the experimental impacted surfaces using *craterslab*. (a) 2D view of the impact surface in the X, Y plane. The fitted ellipse is observed over the distribution of maximum height values around the crater rim. The diameter, which coincides with the major axis of the fitted ellipse, is also represented. (b) 3D visualization of the crater surface. The ellipse that fits over the maximum rim height values is represented by the red line. (c) 3D visualization of the cavity volume, which can be interpreted as the amount of water that can be contained within the crater. This provides a visual interpretation of the numerical value of V_{in}.

Code Availability

Name of the library: *craterslab*

    Contact: frankcm.work@gmail.com and gustavo.vieralopez@gssi.it

    Hardware requirements: Any system compatible with Windows, Linux or MacOS

    Program language: Python 3.10+

    Software required: Python

    Program size: Scripts size – 34.2 kB, pretrained model – 26.3 MB

    The source code is available for downloading at the link: https://github.com/gvieralopez/craterslab

    The data used for this work is available for downloading at the link: https://github.com/gvieralopez/craters-data

    The example codes for craterslab observables analysis are available for downloading at the link: https://github.com/machinfc/Python-Scripts.git

2.4   Morphometric Analysis by Craterslab

In order to validate both, the methodology for studying craters morphologies through ToF sensor and our software library for automating the process, we conducted a set of experiments at different launching heights on a compacted or loose packed sand bed as described in section 2.1, producing a wide range of impact craters types or sand mounds. Figure 2.4 shows the outcomes of three different type of morphologies produced experimentally.

    Figure 2.4a shows the resulting data gathered and visualized using our software for the case of a simple crater, similarly, Figure 2.4b and Figure 2.4c resemble the data from a complex crater and a sand mound respectively. For all three cases, we included an image of the surface taken after the impact. Those images can be seen in Figures 2.4d, 2.4e and 2.4f respectively. When comparing the images in the first and second rows of Figure 2.4, the remarkable similarities between the experimental craters and their three-dimensional visualizations by *craterslab* are evident.

    The images in the third row (Figures 2.4g, 2.4h, 2.4i) depict natural craters on the Moon, Mercury, and Mars, respectively [61, 73, 67]. They were included to highlight the similarities found between our experimental craters and those in our solar system. The insets of these images represent the cross-sectional profiles obtained from the platforms provided by Applied Coherent Technology (ACT) Corporation. Upon comparing the profiles of the images in the second row, obtained by *craterslab*, with those in the third row of Figure 2.4, the striking similarity between granular analog craters and natural craters is remarkable.
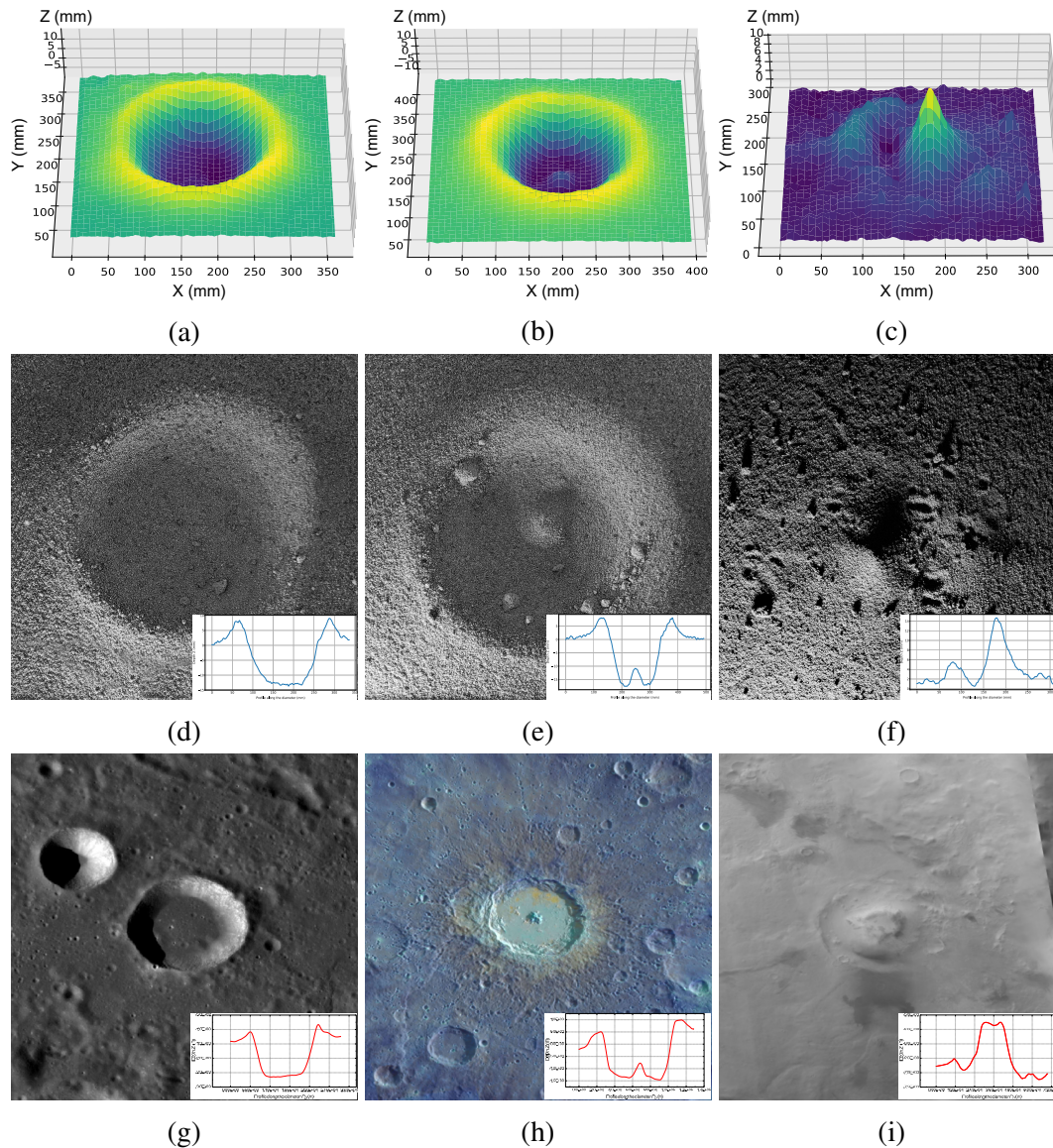
(a)

(b)

(c)

(d)

(e)

(f)

(g)

(h)

(i)

Fig. 2.4 Three-dimensional visualization of granular impact crater morphologies using *craterslab* and Kinect depth data. Experimental and natural craters are compared: (a) Simple crater at 7.0 m above a loosely packed granular bed, $V_{in} = 442966.88 \text{ mm}^3$. (b) Complex crater at 9.0 m above a loosely packed granular bed, $V_{in} = 550837.34 \text{ mm}^3$. (c) Sand mound formed by projectile remnants on a compacted surface at 2.0 m, $V_{exc} = 191267.39 \text{ mm}^3$. Experimental images (d), (e), and (f) correspond to the reconstructed three-dimensional models and serve as a visual comparison, showcasing the similarities and differences between the experimental craters and their reconstructions using ToF sensors. The insets correspond to the cross-sectional profile obtained by *craterslab*. Similarly, images (g), (h), and (i) display natural craters with cross-sectional insets: (g) Simple crater Bernoulli C on the Moon, inset from LROC (Lunar Orbiter Laser Altimeter). (h) Complex crater Debussy on Mercury, inset from USGS DEM (United States Geological Survey Digital Elevation Model). (i) Mound formation on Mars without nomenclature, coordinates: Latitude: −45.47963, Longitude: 55.10807, inset from MOLA DEM (Mars Orbiter Laser Altimeter Digital Elevation Model).
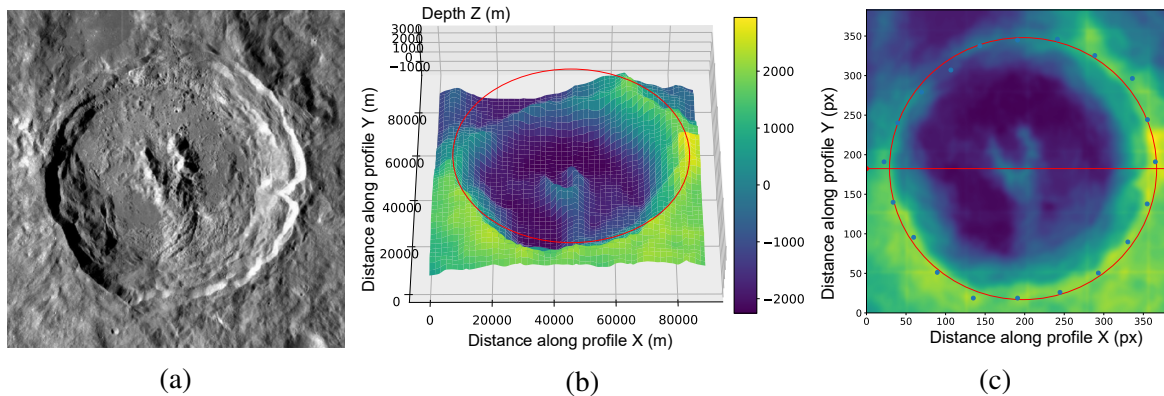
Fig. 2.5 Depth map analysis of the King crater using *craterslab*. (a) King Crater, with a diameter of 77 km and a depth of 5 km, is one of the youngest craters on the far side of the Moon and serves as an excellent example of a Copernican-aged complex impact crater. (b) Three-dimensional projection of King Crater. The volume of its cavity is $V_{in} = 5392.65 \, \text{km}^3$. (c) Two-dimensional representation of the King crater. The highlighted red line indicates the region used to determine the automated profile, which serves as a comparison in Figure 2.6.

In order to expand the evaluation, we proceeded to use our software for analyzing the depth map of the King crater, a well known lunar crater. The results are presented in Figure 2.5, where a three-dimensional visualization of the crater surface with the fitted ellipse on the crater rims (Figure 2.5b) is displayed. In addition to reproducing natural craters in three dimensions and enabling visual analysis, *craterslab* is also capable of extracting the main observables that allow for the analysis of their morphological characteristics.

For the King crater (Figure 2.5a) [58], our software provides results that can be directly compared with those from the LROC platform, such as cross-sectional profile and interior slopes. However, *craterslab* can obtain and analyze additional observables from natural craters, for example the cavity volume (V_{in}).

Additionally, a comparison is shown between the profile view of the crater over the ellipse's largest radii (see Figure 2.5c) obtained by *craterslab* and the profile view by LROC, Figure 2.6. The profile for the King crater obtained by the software is similar to the one obtained by the LROC tool. The slight differences can be attributed to the manual selection of the profile with the LROC tool, which does not allow for obtaining the largest profile from the crater automatically.

Once the 3D data from the experimental or natural craters is obtained, the software can compute the main observables automatically, eliminating the need for manual calculations or laborious image analysis procedures. This automation not only saves time but also ensures a more reliable and consistent analysis, leading to a deeper understanding of the crater morphology and how is correlated with its associated launching parameters.
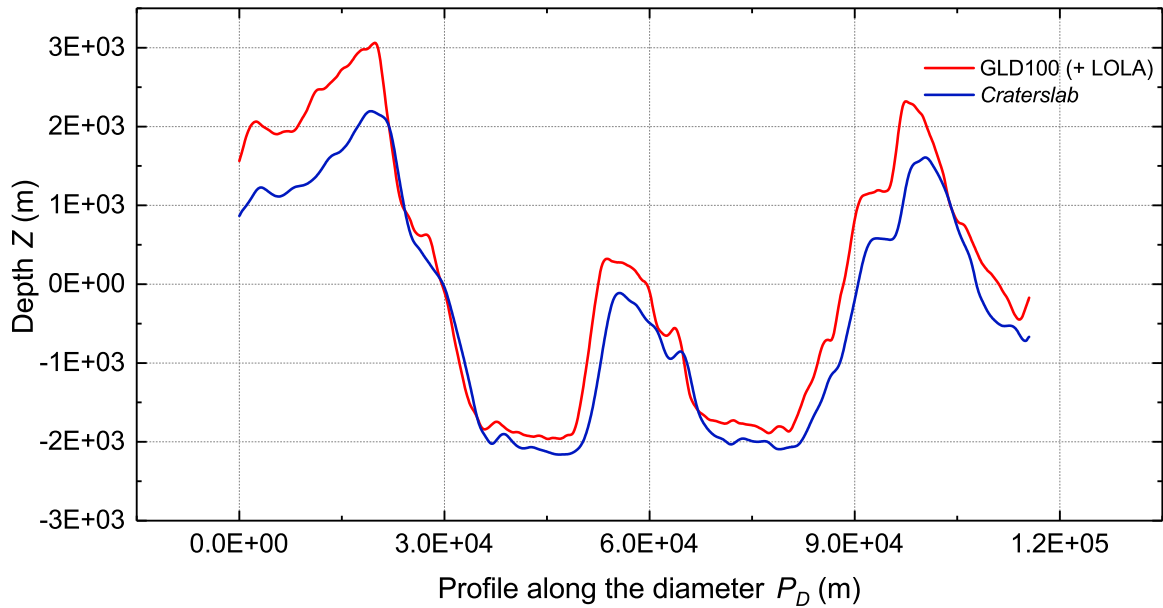
Fig. 2.6 Comparison of cross-sectional profiles of King Crater obtained from the LROC platform using LOLA (Lunar Orbiter Laser Altimeter) and *craterslab*.

Craterslab analyzes information automatically about craters in the solar system, but the reader is cautioned on how to interpret the output data based on the input data. For instance, it is crucial to specify the resolution of the sensor, and in the specific case of information extracted from the ACT platform, consider the geodesy that defines the celestial body in question because it can alter the output values of the software. To address this issue, a function was added to *craterslab* to determine the observables from the surface where the craters are located, not from the geodesy defined on the platforms. More details on this topic can be found in the code examples link https://github.com/machinfc/Python-Scripts.git.

2.4.1   Data Output Validation

Next, we obtain and characterize the morphological variations of the impact surface using our library and a KinectToF as the depth sensor. All craters produced by the collision events were characterized by both techniques: profilometry and software-aided depth map analysis. The morphological characteristics of craters were measured manually from upper view pictures for profilometry, but both manually (MATLAB code) and automatically (Python *craterslab*) from the depth maps provided by the Kinect sensor, for comparison purposes. The main morphological features analyzed are the diameter and depth of the crater; for this reason, data validation will be conducted based on these measurements.

For the Kinect measurements, it was positioned at a height of 102.7 cm perpendicular and stationary to the impact surface. At this working height, for the manual MATLAB method and the automated one on the impact surface, a resolution of 2.8025 mm/px is achieved in the X,Y plane, with ± 1 mm accuracy in the vertical axis. The Kinect camera was calibrated, resulting in a measurement error, for the two-dimensional plane, of ± 0.16 px with respect to the field of view of the infrared camera of 512×424 px [68]. The precision of morphometric features is influenced by the experimental conditions and the sensor's instrumental uncertainty, see subsection 1.5.2. Source code and examples for MATLAB code developed to manually obtain observables are available in https://github.com/machinfc/Matlab-Scripts.git.

X,Y **Plane (Diameter)**

For the KinectToF measurements in the plane X,Y, we first determined the craters diameter manually, mimicking the processing conducted with the profilometry, and then we automatically fitted a rotated ellipse using our software in order to compare both methods for measuring the diameter of the crater (Figure 2.7).

The adjustment parameters shown in the insets of Figures 2.7b and 2.7c reveal an equivalence between both methods regarding diameter, at least for the eccentricity values of these normal incidence impact craters. A slight improvement in the accuracy of the adjustment with *craterslab* is notable in the goodness of fitting. Furthermore, both methodologies for determining the diameter from the depth sensor align similarly with the expected values from the profilometry technique, as seen in Figure 2.7a. The differences between Figures 2.7a and 2.7b are imperceptible, as both methods are manually performed. In contrast, *craterslab* implements a protocol based on the crater's eccentricity to determine the diameter being the diameter equal to twice the major semi-axis of the fitted ellipse, which is impossible to carry out for profilometry and manual depth sensor measurements since a single axis of the laser beam is fixed. At a single height of 4 m, a set of eight identical experiments was performed in order to obtain the relative error of the crater's diameter measurement. These experiments gave a 2.38 % relative error, demonstrating the great reproducibility despite the complex nature of the crater-forming event. The *craterslab* method, being automated, is capable of determining the ellipticity of the crater's rim with small uncertainty by testing a large number of transversal sections of the crater. This cannot be achieved with profilometric techniques unless the process is automated, including image acquisition, laser beam scanning, and image analysis, which is a more complex and cumbersome approach to obtaining the same information. In this regard, ToF (Time-of-Flight) tools are idoneous for acquiring topographic depth maps improving the quality of the measurements, reducing even further their uncertainty and allowing for a more rapid acquisition of the experimental results.

(a) Profilometry method

(b) Manual estimation

(c) *craterslab*
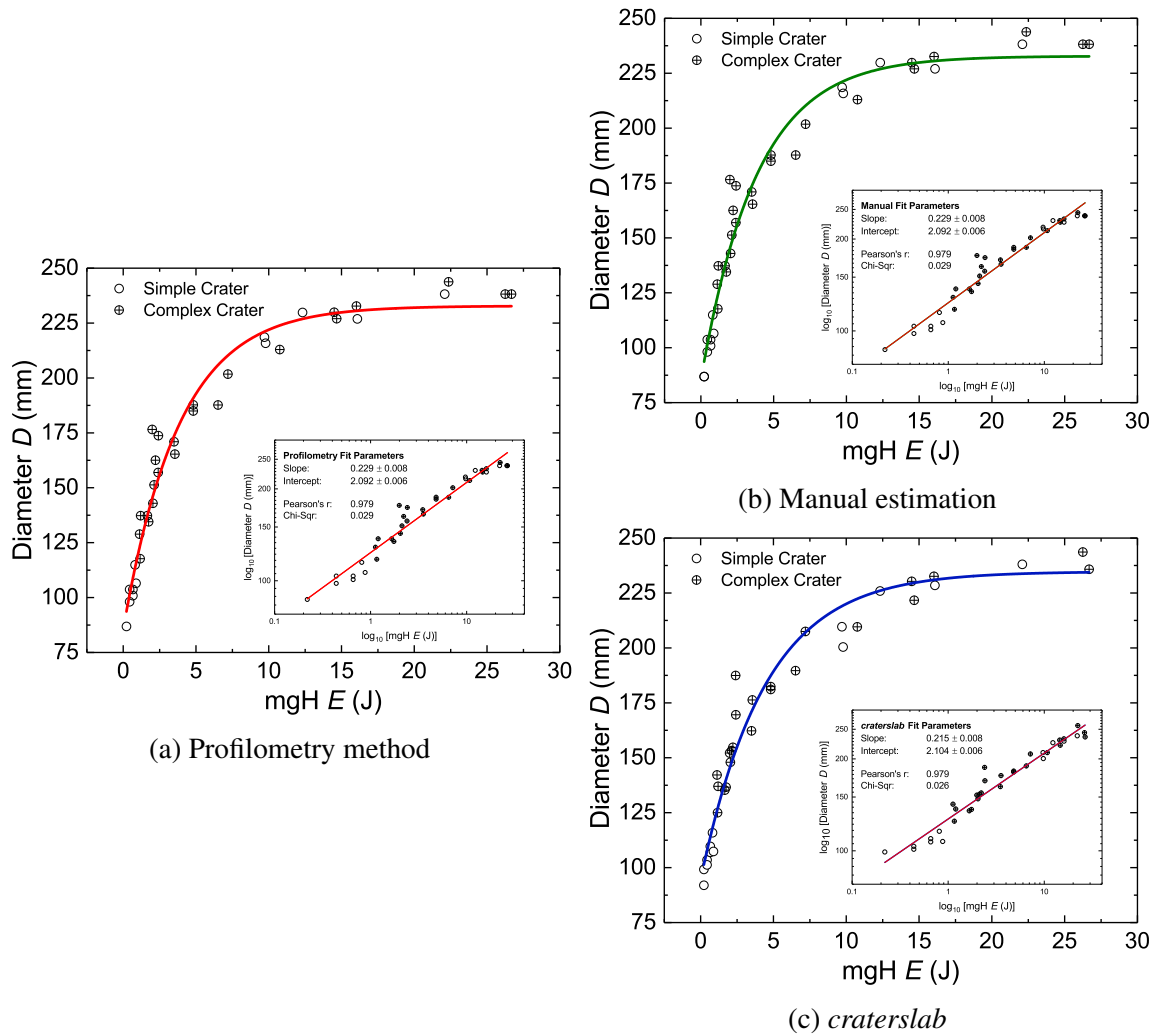
Fig. 2.7 Diameter vs. Potential Energy for Impacts on a Loose Packed Granular Bed. The insets display logarithmic scale plots accompanied by linear fits. All linear fits cases exhibit a slope approximately around ~ 0.22. This preliminary result is close to the exponent found in the relationship $D \propto E^{1/4}$ in low-speed laboratory impact experiments. (a) Diameters obtained using the profilometry method. (b) Diameters estimated manually using Kinect data. (c) Diameters computed automatically using *craterslab*.

Z **Plane (Depth)**

In morphological characterizations involving the *Z* plane, both techniques are equivalent for obtaining depth data but profilometry exhibits a higher margin of error compared to KinectToF. The increased errors in profilometry occur within the interior of the fitted ellipse. This is attributed to the granular nature of the surface and the lighting conditions on the impact surface, which cause the thickness of the laser lines to increase within the crater. This introduces greater uncertainty in the measurement of depth values, as depicted in Figure 2.8. The average thickness in error of the laser lines within the crater is 5.09 mm.

(a)   (b)
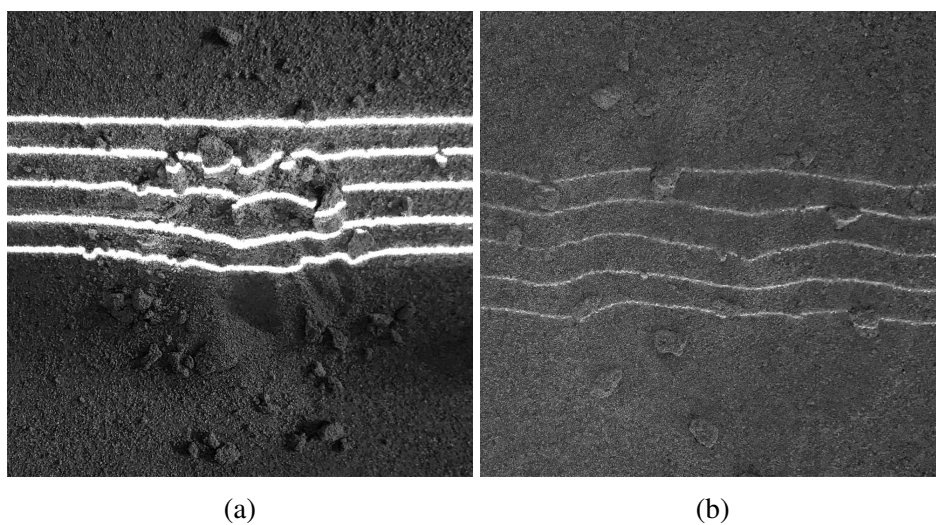
Fig. 2.8 Lines of the laser light beam inside the crater depending on the lighting conditions. (a) thickness 6.96 mm. (b) thickness 3.36 mm.

In contrast, Kinect depth data exhibits an offset of ± 1 mm in our measurements. This offset represents the correction applied to align the depth measurements with the true surface positions, compensating for any systematic errors introduced by the sensor or experimental setup. As a result, Kinect provides higher precision in the three-dimensional reconstruction of granular impact surfaces. Undoubtedly, the *craterslab* library, utilizing Time-of-Flight cameras, stands as a precise and efficient tool for morphological analysis of experimental and planetary impact craters. It provides multiple options for morphometric analysis that raise new questions about the natural processes of crater formation while optimizing work times. In the following chapter, we will delve into morphological and phenomenological analyses of granular-to-granular impact craters.

Chapter 3

Uniaxial Compression Model and Lateral Opening Mechanisms

Remarkable visual phenomenon resulting from the impact of solid or liquid objects on liquid surfaces [89], such as the transient corona-shaped splashes followed by undulating gravity waves, have long captivated observers. These captivating moments were unveiled through high-speed photography techniques pioneered by Harold Edgerton at MIT [16] (for stunning examples, visit https://edgerton.mit.edu/). Conversely, when such impacts occur on the surfaces of solid materials, whether consolidated like granite or unconsolidated like sand, and when the energy involved is sufficiently high, they leave a lasting mark as an indelible scar [81, 47]. This enduring impact, initiated by shock wave propagation and followed by the settling of ejecta, is a fundamental process in the formation and development of celestial bodies, including asteroids, planetesimals, and rocky planets [107]. It is a process that shapes planetary surfaces prior to or in conjunction with other geophysical forces like erosional processes driven by wind and water, radiative heating and cooling (weathering), volcanic activity, and even plate tectonics.

The historical debate concerning the origins of craters, first observed on the Moon's surface by Galileo, was conclusively resolved during the latter half of the 20 th century, thanks to the renewed interest spurred by the Apollo missions and the pioneering work of Jay Melosh [72]. Nevertheless, since Gilbert's experiments in 1893 [37], wherein solid projectiles impacted the surface of sand to model crater formation, questions have lingered regarding the relevance and suitability of these analog models. The primary challenge lies in reconciling the high speeds and energies inherent in planetary crater-forming collisions with the limitations of laboratory experiments, resulting in incomplete or partially overlapping ranges of their corresponding dimensionless scaling parameters.

One aspect of particular interest involves investigating how the packing density of fragile or loosely consolidated granular projectiles influences the ultimate morphological features of resultant craters. This research has yielded intriguing findings, including the formation of central peaks, sometimes accompanied by splashing jets for ultra loose packed targets [82].

However, it is not merely a matter of having equal dimensionless scaling numbers (such as the ratio of gravitational to dynamic pressures, described by the Froude number: $F_r = gd/2v^2$); it is equally crucial to replicate the same scaling laws observed in planetary objects during terrestrial experiments. Each type of experiment, whether involving explosions, hypervelocity impacts, or low-energy scenarios, exhibits its distinct signature in the scaling laws that describe its morphology.

Nahmad and colleagues [10] have highlighted both, the differences and similarities in the scaling laws governing the morphological features of craters in planetary and laboratory settings. They observed that hypervelocity impacts, explosions, and solid objects penetrating loosely packed sand form craters with different power law relationships for aspect ratios (volume vs. diameter) compared to craters formed by impacts of fragile projectiles or those observed on celestial bodies like the Moon, Ganymede, and Callisto.

Their findings have raised questions about the role played by the relative strength and packing between the target and the projectile, which is a central focus of our present study. Furthermore, their observations have revealed that as impact energy increases, the depth of craters saturates but is still an open problem for solid or granular impacts on tightly packed targets or the underlying physical mechanisms of saturation of depth remain unexplained. In this context, our experiments aim to systematically investigate and comprehend how target material strength and compaction influence the final morphology of craters.

By proposing a Heckel's uniaxial compaction mechanism, where the compressibility of the target is proportional to its porosity, we model the impact and deposition of the projectile onto the target surface. This model enables us to accurately describe the compressive subsidence of the crater's floor caused by the dynamic pressure exerted by the impacting projectile. Similarly, a crater opening mechanism is presented, which raises new questions through the morphometric exploration of the craters.

3.1 Crater Depth Prediction in Granular Collisions

In Figure 3.1 subsequent pictures of the crater formed by the impact of sand lump-like projectiles are presented. Figure 3.1a depicts a loose packed sand target, while Figure 3.1b shows the case of a compacted sand target. In both scenarios, as the energy increases the projectiles crumbles in smaller pieces, excavating a larger and deeper crater.
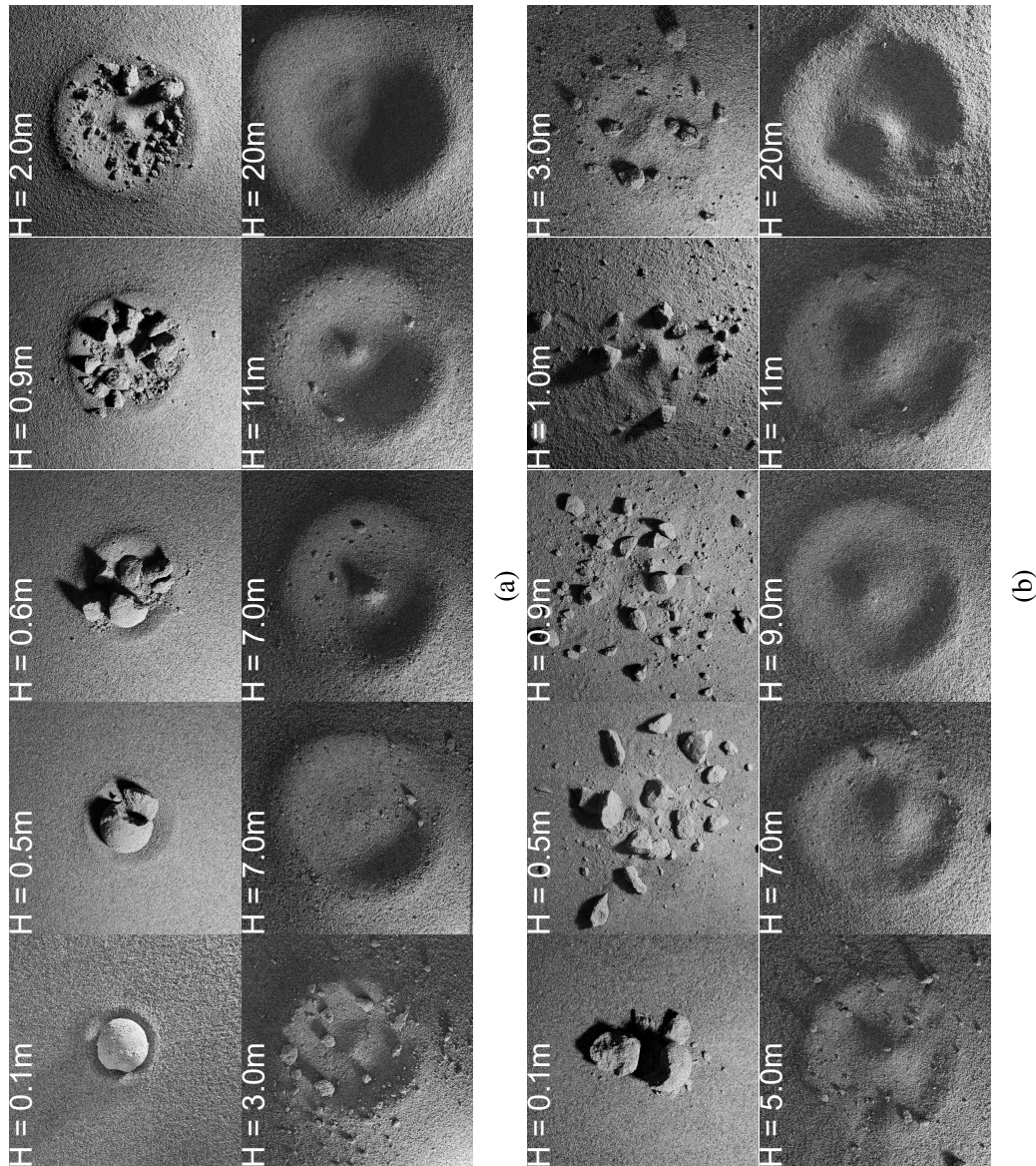
(a)

(b)

Fig. 3.1 Subsequent pictures of the crater formed by the impact of granular projectiles at different heights. (a) For a loosely packed sand bed and (b) for a compacted sand bed

The sequence of craters formed for increasing energy in a loosely packed target, as shown at the beginning in Figure 3.1, clearly illustrates the crater formation process driven by the displacement volume of target material due to the partial penetration of the intact projectile for low energies (note deeper craters before fragmentation than immediately after). As the dropping of height gradually increases, the crater diameter grows, and simultaneously, the projectile breaks down into smaller fragments, progressively filling the crater's bottom. With a further increase in collision energy, the diameter continues to enlarge, leading to the formation of a central peak or dome and ejecting more (and smaller) projectile fragments out of the crater's rim.

In contrast, for the compacted target terrain, as illustrated in the second row of Figure 3.1, the sequence initiates with the projectile breaking apart at lower dropping heights, resulting in an absence of noticeable crater excavation at low energies. The lower section of the projectile, which experiences the majority of the impact, is pulverized and remains confined on top of the target's terrain due to the dynamic pressure exerted by the avalanche of larger projectile fragments [82, 9]. The confined pulverized portion of the projectile forms a mound on top of the target terrain, and it is surrounded by scattered projectile fragments, see Figures 1 and 2a in [82]. A clearly distinguishable crater is not formed until the collision excavates below the ground surface. Therefore, we consider a circular region containing most (approximately 90 percent) of the remaining mound material by searching the limits at which the terrain do not present further elevation with respect to the ground level. The diameter of this region is defined as the diameter of the mound. These mounds will be represented with triangular symbols in our plots.

These mounds are the precursors to the central peaks that will appear in excavated craters once the energy overpass the threshold required for which the impact excavates below the ground surface. The larger fragments (representing less than approximately 1/20 part of the projectile diameter) that are not considered part of the mound progressively decrease in size and scatter further away from the impact point as the dropping energy increases. The crater begins to exhibit a subtle rim and a central peak increasing its depth as the energy grows. At sufficiently high energies, the crater appears to replicate the growth process observed in loosely packed sand craters, but with smaller diameters and depths.

The complex craters obtained in experiments with granular impactors against granular surfaces are flat, like tortillas, with tall central peaks. Every crater formed on compacted targets has a central peak, while a few, randomly distributed, of the craters formed on loosely packed targets lack this feature as can be seen in Figure 3.1 and marked as hollow symbols in other figures.

3.1.1   Uehara's Depth Model

The depth of the crater being one of the central issues of this research, we plotted the maximal depth of excavated craters as a function of energy, in which we found two regimes. This abrupt transition between depth regimes is characterized by differing behaviors, see Figure 3.2, with our emphasis on the second regime. The first regime occurs at lower dropping heights for both loosely (from 0.1 m to 1.0 m) and compacted (from 0.1 m to 3.0 m) sandbox targets respectively, while the second regime takes place at higher dropping heights.
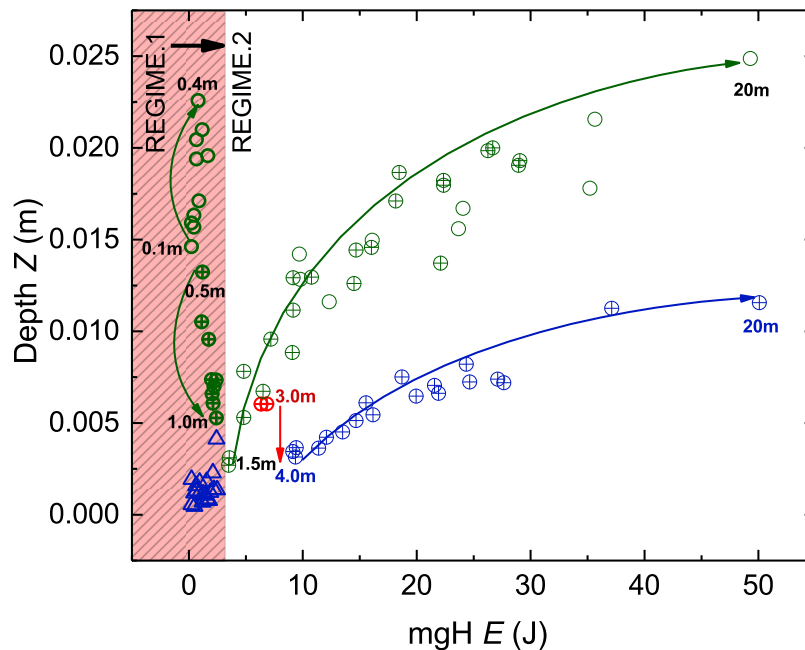

Fig. 3.2 This figure represents the transition between depth regimes in crater formation for loosely (green symbols) and compacted (blue symbols) sandbox targets. Sand mounds are represented by △, simple crater formation by ○, and complex crater formation by ⊕. The symbols inside the red area correspond to the first regime. In the second regime, the symbols ⊕ belong to experiments on compacted sandbox targets but are excluded from the data because they represent data from the first regime (at a height of 3.0 m), although they are not located within the red area. The arrows represent a visual guide of the evolution of depth while varying the dropping height for both experimental sets.

   This transition from one regime to other stands for the fragmentation of the projectile as the dynamic pressure of the projectile at impact overcomes its own yield stress. The comminuted material deposits, partially filling the just opened crater, and thus producing a non-monotonic behaviour of the depth as a function of dropping energy. In the same Figure 3.2, the first regime in which the projectile has preserved integrity, or at least part of it, is remarked with a reddish color. From here on, it's important to note that data in

some graphs represent only a fraction of the complete dataset due to the observation of these different regimes, and we will focus mainly at the regime after the fragmentation transition just described has overcome.

Examining the depth's dependence on impact energy, see Figure 3.3, at the light of Uehara model who also defines a universal law for depth of the crater vs impacting energy, given by:

$$Z = 0.16[\rho_b/(\rho_g\mu^2)]^{1/2}D_b^{2/3}H^{1/3} \tag{3.1}$$
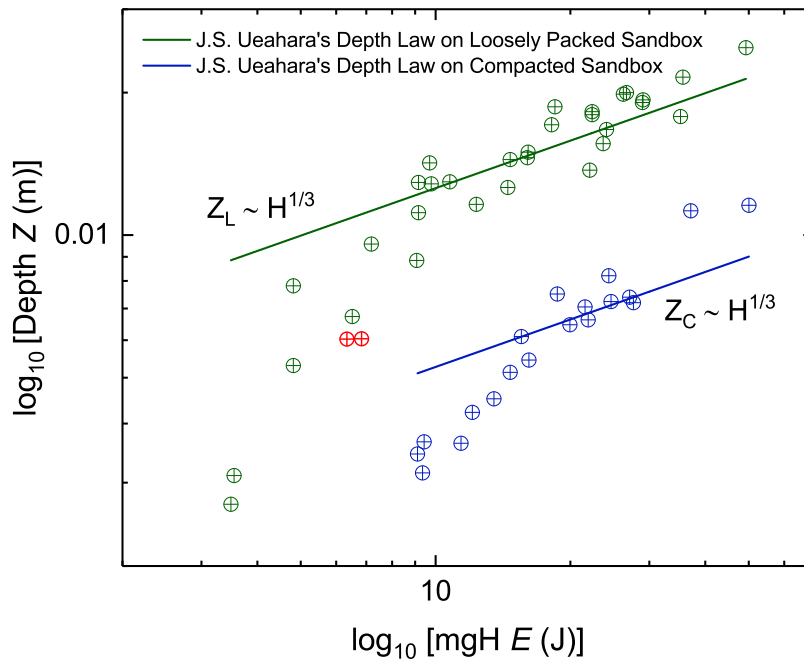

Fig. 3.3 Uehara's Law for depth growth as a function of impact energy. The symbols ○ represent simple crater formation, ⊕ represent complex crater formation, and ⊕ represent excluded data points from experiments on a compacted sandbox target, which are part of the first depth regime.

This result of Equation 3.1 is observed for craters formed by solid balls dropped into dry, non-cohesive, granular media, where the ball's density ρ_b, its diameter D_b, and the dropping height H are varied. The model employed is based on a regime when the energy is dissipated by plastic flow of the medium throughout a volume proportional to the cratre's diameter ($\sim D_c^3$).

Then, one gets the results shown in Figure 3.3, where we performed a fit using Equation 3.1, with the static friction coefficient as a free parameter following the same procedure as will be employed in the diameter fitting, in this case, $\arctan\mu = \theta$. Clearly, as observed,

the Uehara model for depth as a function of impact energy poorly fits our experiments on both loosely and compacted sandbox targets, and the values of our free parameter deviate significantly ($\theta = 73.1°$ on loosely packed sand and $\theta = 82.8°$ on compacted sand) from the real friction coefficient measured. Figure 3.3 does not adhere to a power-law relationship, and the Uehara model is not capable of describing the growth of depth with impacting energy.

Based on observations of granular impactors against granular impact surfaces, such as the experiments in 2D performed by Bartali *et al.* [9], in which the crumbled or pulverized projectile acts more like a piston compressing the target's terrain, we can observe that the depression forming the crater's bottom is caused by subsidence of the free surface of the target due to the compressive stress exerted by the projectile impact.

Following the mechanism revealed by these 2D experiments, we propose a uniaxial compaction process occurring vertically in order to explain the depth-energy relationship, mechanism which does not align with the volume displacement model from which Equation 3.1 was derived.

As a note, the depth values used in the fitting of Equation 3.1 in Figure 3.3 correspond to the excavation depth (d_{exc}). Counterintuitively, when performing this fit on depth values from the rim height of the crater to the maximum depression inside (d_{max} see Figure 2.1), the Uehara fit for depth improves.This phenomenon may arise because his model is predicated upon impacts involving solid projectiles, consequently augmenting the depth values. This constitutes an intriguing facet warranting further investigation, and we leave it as an open topic for future research.

3.1.2   Heckel's Model

In order to explain the depth vs energy dependence, we propose a compaction model based on Heckel's law [41], commonly used in the pharmaceutical industry [53], where a solid piston compacts a granular medium. However, in our case, we would be dealing with a porous piston made of sand, which is part of the pulverized granular projectile. Thus, according to Heckel's law, the compressibility of our granular sandbox target will be proportional to its porosity. Therefore, the available space for compaction can be expressed as:

$$\frac{d\phi}{dP} = K(\phi_{\mathrm{max}} - \phi) \tag{3.2}$$

Where ϕ is the volume fraction of the target, P is the pressure, K is a constant and ϕ_{max} is the maximum packing fraction of the granular medium. By integrating Equation 3.2 it transforms into:

$$\phi = \phi_{\text{max}} - (\phi_{\text{max}} - \phi_0)\exp^{-K(P-P_0)} \tag{3.3}$$

Where K is a free parameter, which we will refer to as the compacting susceptibility of the granular medium, ϕ_0 is the packing fraction of the medium before experiencing uniaxial compressive stress, ϕ_{max} is the maximum packing fraction the medium reaches when subjected to vertical dynamic pressure P, and P_0 is the initial dynamic pressure, which in our case corresponds to the pressure the medium experiences when the projectile hits the target $P_0 = \rho v^2/2$, being v the impact velocity and ρ the projectile's density.

In order to corroborate Equation 3.3, we will transform the axes of Figure 3.3 from depth Z to packing fraction ϕ and from energy E to the dynamic pressure P applied to the target.

Firstly, we define the packing fraction (ϕ). This parameter characterizes the spatial arrangement of granular ensembles and is expressed as the ratio of the volume occupied solely by the grains to the total volume encompassed by the ensemble, accounting for the interstitial voids among individual grains. An alternative formulation of the packing fraction involves the quotient of the density of the granular ensemble (ρ_{GP}) divided by the density of the solid material (ρ_s) composing the grains, expressed as $\phi = \rho_{\text{GP}}/\rho_s$.

For a vertical cylindrical container with a cross-sectional area A and height h, filled to its rim with granular material, we define its density ρ_0. This density corresponds to the initial density of the ensemble before impact, denoted either as ρ_L for a loosely packed medium or ρ_C for a compacted one. ρ_0 is determined by dividing the mass m of the granular material by the product of the cross-sectional area and the height, $A \cdot h$.

Subsequently, if we uniformly compress the granulate along its vertical axis by a distance Z, while maintaining the transverse section, we achieve a granular packing with a new density given by $\rho_{\text{GP}}(Z) = m/A(h-Z)$. However, it's important to note that we are simplifying by assuming uniform compaction throughout the granulate. In reality, compressive stress induces a density gradient within the granular material [40].

The quotient of these two densities is expressed as:

$$\frac{\rho_{\text{GP}}(Z)}{\rho_0} = \frac{h}{h-Z} \tag{3.4}$$

Finally, from the second definition of the packing fraction and the Equation 3.4, we obtain:

$$\phi(Z) = \frac{\rho_0}{\rho_s}\frac{h}{h-Z} \tag{3.5}$$

it can be noted that Z aquires its maximum allowed value when the density of the granular ensemble reaches the closest packing achievable. Since we are dealing with non-deformable

grains, the final packing fraction would be a complex function of the shape and size distribution of grains. For example, a set of identical spheres randomly packed would achieve a volume fraction of 0.64 while for a perfectly ordered array of identical hard spheres it will reach a 0.74.

On the other hand, the impact energy per unit volume is essentially the dynamic pressure, denoted as $P = \rho g H$. This concept can be likened to the pressure exerted by a vertical water (sand) jet striking the sandbox target, where the area in which momentum is transferred is considered as the constant transversal section of our projectile.

By using Equation 3.5, to transform our values of depth Z into volume fractions ϕ, and using the relationship of dynamic pressure as a function of the energy to plot ϕ vs P, Figure 3.3 gives rise to Figure 3.4, displaying the fit of Equation 3.3 for the second regime for both loosely packed and compacted sandbox targets, each with its respective free parameters K_L and K_C.
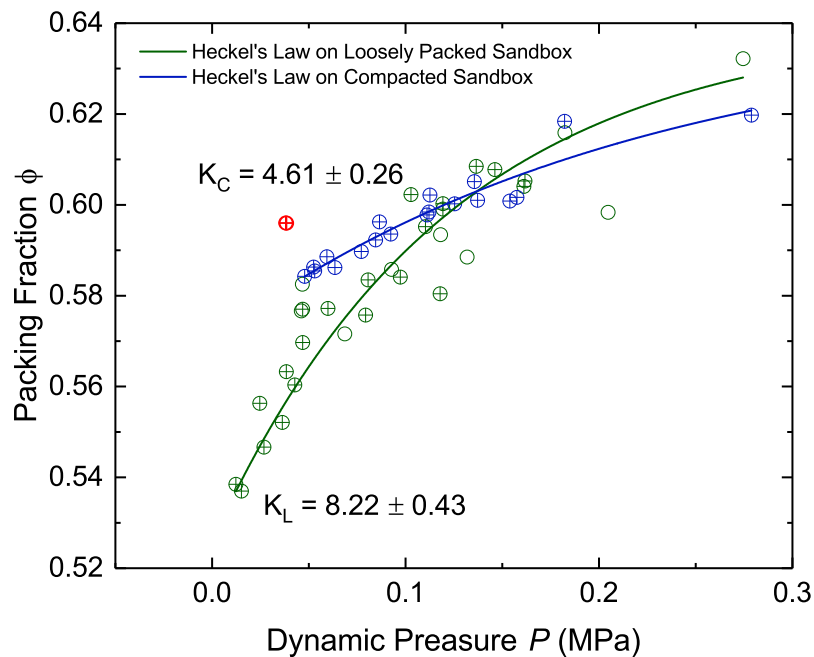

Fig. 3.4 Heckel Compaction Model for both loosely packed and compacted target. The symbols ⊕ represent excluded data points from experiments on a compacted target, which are part of the first energy vs depth regime.

The Heckel-based model elucidates the saturation of depth through a compaction mechanism, tending to a filling fraction equal to random close packing, $\phi_{RCP} = 0.64$ [7], employing an exponential law. The compacting susceptibilities, K_L and K_C, offer insights into the medium's easiness of compacting as the dynamic pressure increases. In this context, K_L is nearly twice that of K_C.

On the other hand, the primary reason for these differing susceptibilities, K_L and K_C, is better explained by the way in which projectile fragments are more easily expelled horizontally with the ejecta for compacted targets compared to loosely packed ones. This phenomenon was observed during experiments where the ejected material was thrown away from the impact zone much faster in compacted targets than in loosely packed targets for the same impacting energy as can be seeing in Figure 3.5 and Supplementary Materials in Appendix A.
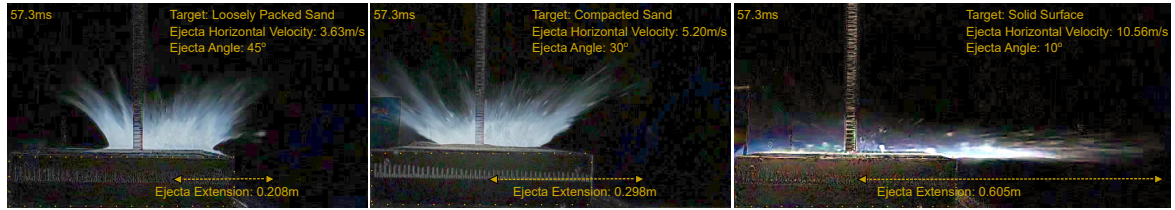

Fig. 3.5 From left to right, differential images of the ejecta taken at 57.3 ms after first impact for loosely packed, compactly packed, and solid targets respectively.

To verify this phenomenon, side-view videos of the impact zone were captured at 960 frames per second (fps), and the velocities of the material ejection and the displacement of the crater opening ejecta crown were measured. Upon conducting an analysis of these videos, it was determined that an ejection angle with respect to the horizontal of $45°$ for loosely packed targets, a $30°$ for compacted targets and less than $10°$ for a solid target corroborates a larger vertical to horizontal coefficients of momentum transfer for compacted versus loosely packed targets. Besides a horizontal speed of the ejecta of 3.63 m/s, 5.20 m/s, and 10.56 m/s for loosely, compacted and solid targets respectively were measured.

Let's now make an analysis using a simple energy balance for assessing the energy spent in opening the craters in each case.

3.1.3 Energy Balance

Assuming the effective stopping force F_r as constant during the subsidence of the crater's floor, and the fraction of energy transferred from vertical to horizontal $\kappa_{vh}mgH$, where κ_{vh} stands for a transferred coefficient of vertical to horizontal momentum, thus the conservation of energy must satisfy:

$$\kappa_{vh}mgH + \int_0^Z F_r dl = mgH \tag{3.6}$$

This is nothing more than the work done by the frictional force plus the energy of the ejected material as a function of impact energy. We can assume that the frictional force is a

drag force proportional to the area of the crater's floor $F_r \propto \mu_e A_c \propto \mu_e D^2$, where μ_e is the effective friction coefficient of the packing and A_c is the area of the crater's floor. Therefore, Equation 3.6 transforms into:

$$D^2 Z \propto \frac{1 - \kappa_{vh}}{\mu_e} mgH \qquad (3.7)$$

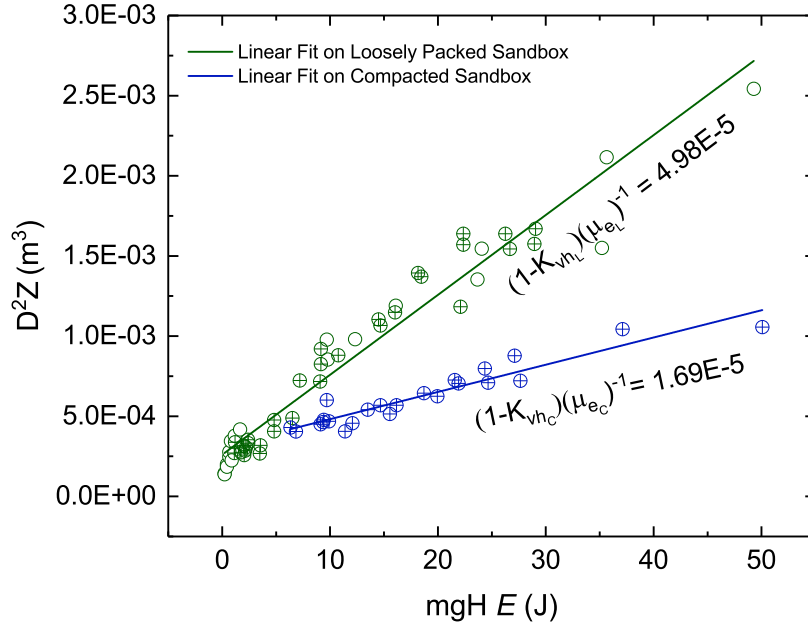

Fig. 3.6 Energy balance between stopping forces proportional to D^2Z in relation to the impact energy. The vertical momentum transfer to horizontal is higher for compacted sandbox targets.

Figure 3.6 shows the energy balance approximation. It can be observed that the slope of the loosely packed experiments (in green) is nearly three times the slope for compacted experiments.

However, considering that the effective friction coefficient tends to increase as the density of the granular packing increases due to grains tending to be more closely packed [126], then the effective friction coefficients can be expressed proportionally to their respective densities of the loosely packed and compacted sand media as follows: $\mu_{eL} \propto \rho_L = 1.39 \, \text{g/cm}^3$ and $\mu_{eC} \propto \rho_C = 1.52 \, \text{g/cm}^3$. In this way, we can resolve the slopes of Figure 3.6, and it can be deduced that $\kappa_{vhC} > \kappa_{vhL}$.

This result remains consistent with compaction susceptibility determinations, where their differences are attributed to the mechanism of greater transfer of vertical momentum to horizontal momentum in compacted sandbox compared to loosely packed sandbox. The

energy balance not only confirms this more efficient transfer mechanism but also offers a physical model for understanding the crater formation process.

Upon impact, several processes unfold. The projectile first penetrates the target until the dynamic pressure reaches its yield stress, resulting in fragmentation and the formation of a "porous piston" made of pulverized sand. This porous piston exerts pressure on the receding target surface, while stresses propagate downward, compacting the target material producing subsidence of the crater's floor, and establishing a compaction gradient below [40]. Simultaneously a central mound or peak develops, which is the lower part of the projectile trapped between the crater's floor and the rest of the projectile flowing downward due to dynamic pressure [3].

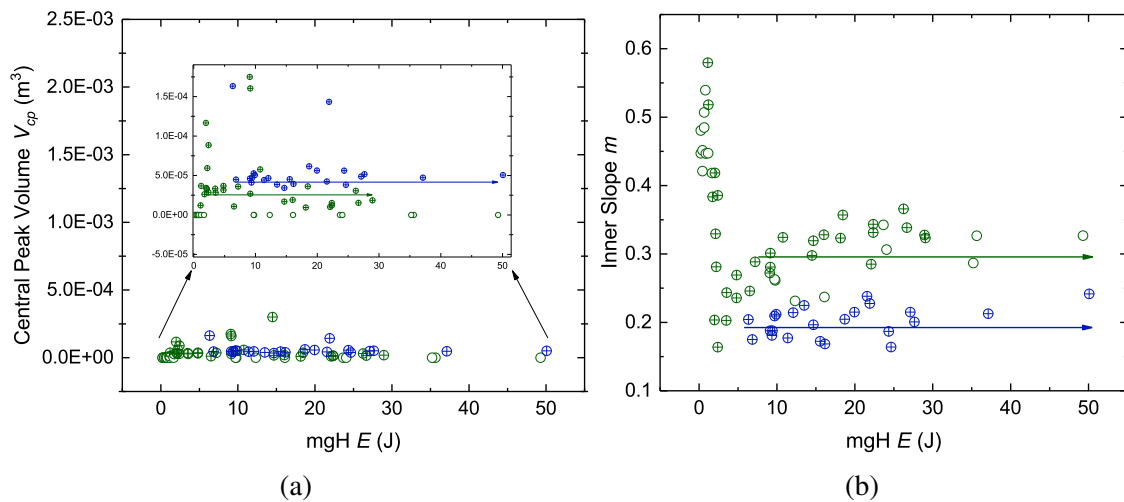(a)   (b)

Fig. 3.7 Saturation of the interior slopes of the crater and the volume of the central peak concerning energy input is observed. Both figures support the model of horizontal-to-vertical momentum transfer, indicating a greater enhancement of horizontal momentum for compacted sandbox experiments.
(a) The inset in this figure provides a closer view of the data overlay from experiments with loosely packed and compacted sand. It is evident that, in both cases, the volumes of the central peaks saturate. Moreover, the central peaks in compacted sandbox experiments are larger than those in loosely packed sandbox experiments, probably promoting more efficient vertical-to-horizontal momentum transfer in compacted sandbox experiments. (b) In both cases, there is a saturation of the interior slopes of the craters. It is confirmed that the craters formed in compacted sandbox experiments are flatter (with lower interior slopes) compared to those in loosely packed sandbox experiments. The arrows serve as a visual guide to highlight the saturation of the inner slopes in both experimental groups.

We consider that friction plays a significant role in the compaction processes of both loosely and tightly packed sandbox targets [29], but we still lack a clear understanding of its relationship with compacting susceptibility. We acknowledge that there are distinctions

between the macroscopic mechanisms we describe and the actual microscale processes [15] that lead to the effective friction coefficient we utilize.

In our experiments with compacted sand, we observe shallower craters with lower rims and smaller diameters compared to those formed in loosely compacted targets. The projectile hardly excavates below the ground surface, and a larger mound or central peak is more easily formed, in comparison to loosely packed targets, peaks that likely promote a better vertical to horizontal transfer of momentum: these two phenomena makes smother inner rim slopes, see Figure 3.7b, precluding further radial growth of the crater (smaller diameters than in loosely packed targets for the same energy). Further investigation is warranted to elucidate the mechanism underlying the increased backscattering of ejecta from loosely packed targets compared to more densely compacted or solid targets.

As a remark, let us say that the Uehara model describes a different physical system than our experiments in the sense that for solid vs granular collisions there is no compaction of the target in the vertical direction, but instead a penetration of a solid into a dense gas of solid particles followed by evacuation of certain amount of material. In contrast, for fragile softly consolidated aggregates of sand the projectile crumbles into small fragments upon the impact and spreads over a larger area than the projectile's cross section, pressing down and causing a compressive subsidence of the target's terrain. Thus it is natural that the Uehara's model does not describe accurately the vertical excavation of our experiments.

However, in granular collisions part of the energy is diverted towards horizontal degrees of freedom in the same way as the displaced material from a solid vs granular collision and some correspondence can be expected among granular lumps vs. granular targets and solid vs. granular targets craters for the predicted diameter. This horizontally diverted material produces the ejecta and contributes to the formation of the crater's rims.

3.2   Opening Mechanisms: A Morphometric Exploration

Once we have delved into the saturation of impact crater depth in the granular-granular type, let's proceed with a more detailed morphometric analysis. Figure 3.8, similar to Figure 3.1, illustrates the morphological evolution of the craters as the impact energy increases. In this instance, the diameter profiles, detected by the *craterslab* library, have been integrated, keeping depth to scale, to examine their aspect ratio. This is of great importance because these are the primary observational measures used to describe planetary craters. This analysis will be conducted later on.

As observed in the first row of Figure 3.8, the depth increases significantly more in the experiments involving loosely packed sand compared to the second row of this image, which

includes experiments related to compacted sandbox, a topic already discussed in Section 3.1. Regarding the diameter, we can see that it is slightly larger in experiments with loosely packed sandbox (Figure 3.8a) compared to those with compacted sandbox (Figure 3.8b). Both experimental groups present well-defined differences in their morphologies, yet, from certain impact energies onwards, the diameters are not as dissimilar. What are the opening mechanisms involved in these events?
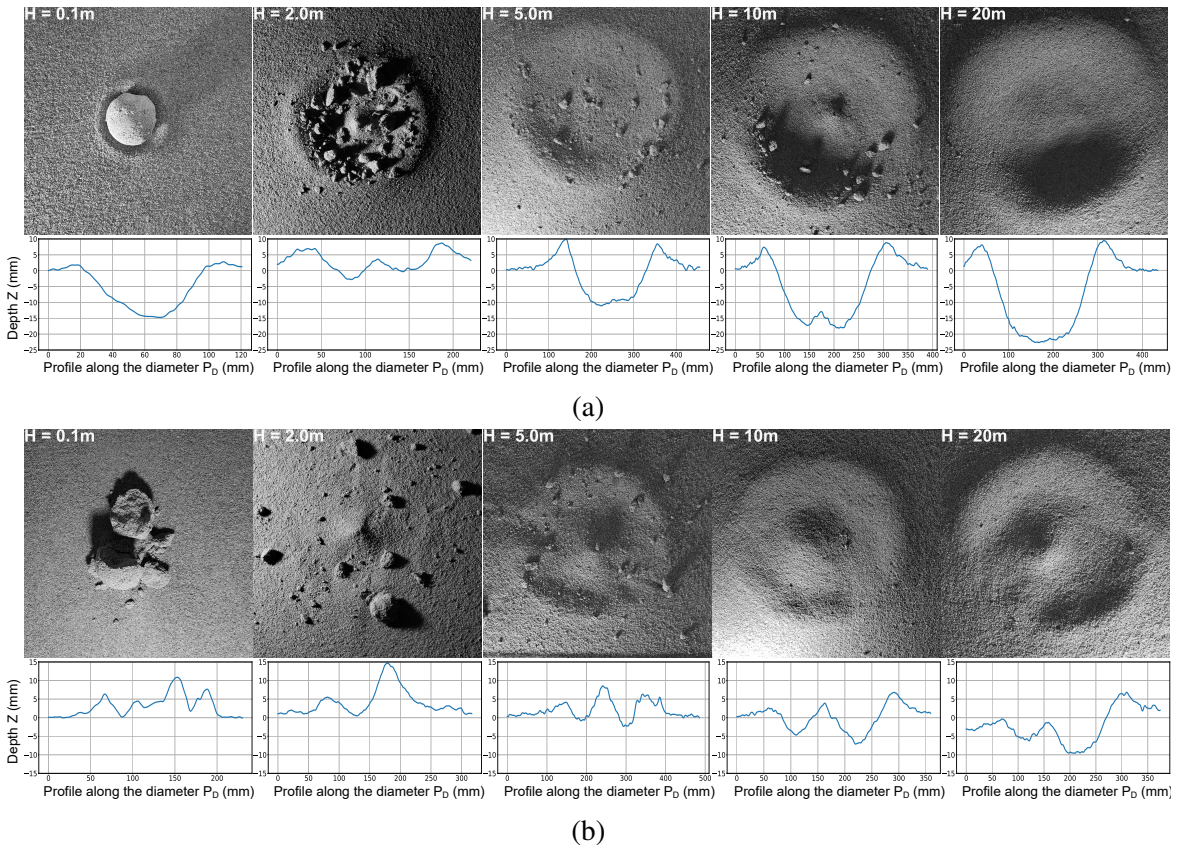

(a)

(b)

Fig. 3.8 Short evolution of impact craters on loosely packed and compacted sandbox varying impact energy. Below each picture a transversal section provided by the *craterslab* library is shown to give a visual idea of the crater morphology. Only lateral dimensions scales are different, while vertical scale remains the same for all craters presented, showing the non-monotonic trend of depth as a function of energy due to the transition that occurs when the projectile breaks apart. (a) For a loosely packed sand bed, and (b) for a compacted sand bed.

3.2.1   Uehara's Diameter Model

Let's now analyze the growth of the crater diameter (D) as a function of impact energy. Uehara and coworkers [109] reports that the crater diameter scales with an exponent of $1/4$

concerning the projectile's impact energy as a universal law, as shown in Equation 3.8. This result is observed for craters formed by solid balls dropped into dry, non-cohesive, granular media, where the ball's density ρ_b, its diameter D_b, and the dropping height H are varied. The model employed is based on a "gravity-limited" regime, where the energy is primarily utilized to lift a volume of $\sim D^3$ to a height of $\sim D$ against the force of gravity.

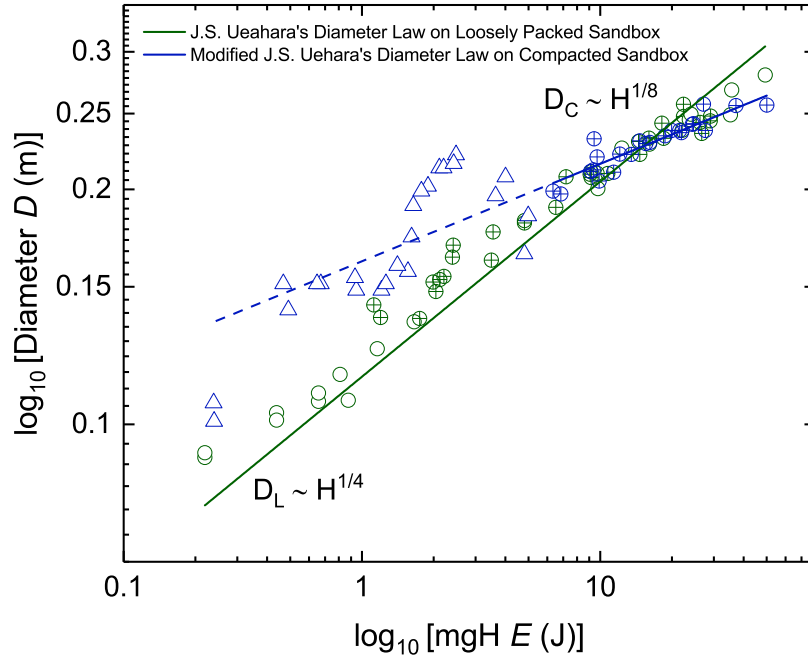$$D = 0.92[\rho_b/(\rho_g\mu^2)]^{1/4}D_b^{3/4}H^{1/4} \qquad (3.8)$$

Fig. 3.9 Uehara's Law for diameter growth as a function of impact energy in experiments on loosely packed and compacted sandbox targets. The symbols $\triangle$ represent sand mounds, $\bigcirc$ represent simple crater formation, and $\oplus$ represent complex crater formation. The diameters presented for sand mound events corresponding to compacted sandbox experiments were obtained through manual estimations using the algorithm developed in Matlab. Although these events do not correspond to crater formation (ranging from $0.1 - 2.0\,\text{m}$ in drop height) due to the absence of penetration into the impact surface, their diameters are determined because a gradual growth is observed. This representation of diameter increase can be associated with the energy required to reach a critical level that allows excavation on the surface to enable crater formation. For example, on Mars, such morphologies indicating low-energy impacts can be found. Ultimately, they are included because their gradual growth before and after surpassing the yield strength of the surface is interesting, providing a larger dataset for a more robust statistical analysis.

Additionally, Pacheco and colleagues [82] made experiments similar to those conducted by Uehara while using granular projectiles with varying porosity and keeping their diameter

constant. Interestingly, certain similarities were observed with craters morphologies produced by solid spheres since both obey the scaling law proposed by Uehara for the crater diameter. However, Pacheco *et al.* extended the Uehara law for diameter versus energy to describe the appearance of a gap between the diameters, employing Equation 3.9.

$$D = C[\rho_b/(\rho_g)]^{1/4}D_b^{3/4}H^{1/4} + (\Delta D)\Theta(H - H_f) \tag{3.9}$$

Figure 3.9 represents the diameter as a function of energy for our experiments in loosely or compacted packed sandbox targets. In no case did we observe a gap between the diameters described in the equation3.9. For this reason, we proceed to fit the data using the Uehara equation for diameter (Equation 3.8) with the static friction coefficient μ as a free parameter. The rest, including the density and diameter of the impactor, and the density of the granular medium, were fixed to our experimental data. In the case of loosely packed sand, Equation 3.8 fits well, and a slope angle ($\arctan\mu = \theta$) is obtained for the free parameter of $\theta = 40.2°$, which aligns with the angle of repose of our granular medium.

However, when applying the same procedure to the data from compacted sandbox targets, we found that Equation 3.8 does not fit accurately with a coefficient of determination COD or a R-squared value of $R^2 = 0.082$. Nevertheless, by modifying one of its exponents to the form $D \sim H^{1/8}$, the fit improves significantly. This exponent is suggested by the best fit of the data. By making this modification to Equation 3.8 and fitting it to the data, we achieve a good fit ($R^2 = 0.82$) but a low angle of repose of $\theta = 23.2°$ which does not correspond to the angle of repose of our granular medium.

In the fitting process for this experimental group, the data from sand mounds are not considered since they do not correspond to crater formation due to the absence of penetration into the impact surface. Nonetheless, their diameters are determined based on our criteria and included in Figure 3.9 because a gradual growth is observed. This diameter increase can be associated with the energy required to reach a critical level that allows excavation on the surface for crater formation. Ultimately, their gradual growth before and after surpassing the yield strength of the surface is interesting.

It can be asserted that the dependence of diameter on impact energy for a loosely packed surface adheres to Uehara's law because it follows the volume displacement model for a "gravity-limited" regime. However, for a compacted surface, even though it still exhibits a power-law relationship, this regime undergoes some a notorious change in the exponent, showing an still unknown underlying physical mechanism preventing the diameter from increasing in the same manner.

The universal model proposed by Uehara has been the guiding principle for determining the relationship between diameter and impact energy, i.e., the mechanism of lateral opening

of craters. Moreover, it has been experimentally verified by multiple authors. Later on, as part of the morphometric exploration, we will revisit this topic in Subsection 3.2.5.

3.2.2 Aspect Ratio

As previously discussed, the depth transitions between two energy regimes, as seen in Figure 3.2, where the morphology of the craters changes, sometimes abruptly. This behavior, attributed to the deposition of impactor remnants, is observed in Figure 3.10, where the aspect ratio is analyzed. In the case of loosely packed sand, it seems that we are witnessing three regimes, while in the case of compacted sand, two regimes are maintained.

In our experiments, we will focus on the case of loosely packed sand, specifically on the aspect ratios between dropping heights of $0.1 - 0.4$ m and $1.5 - 20$ m. The data between dropping heights of $0.5 - 1$ m contains a significant portion of impactor remnants; for this reason, they are not considered for analysis. In compacted sandbox experiments, we will continue to focus on the second regime because, in the first regime, the impact energies do not exceed the yield strength of the impact surface, and there is no visible penetration into it.
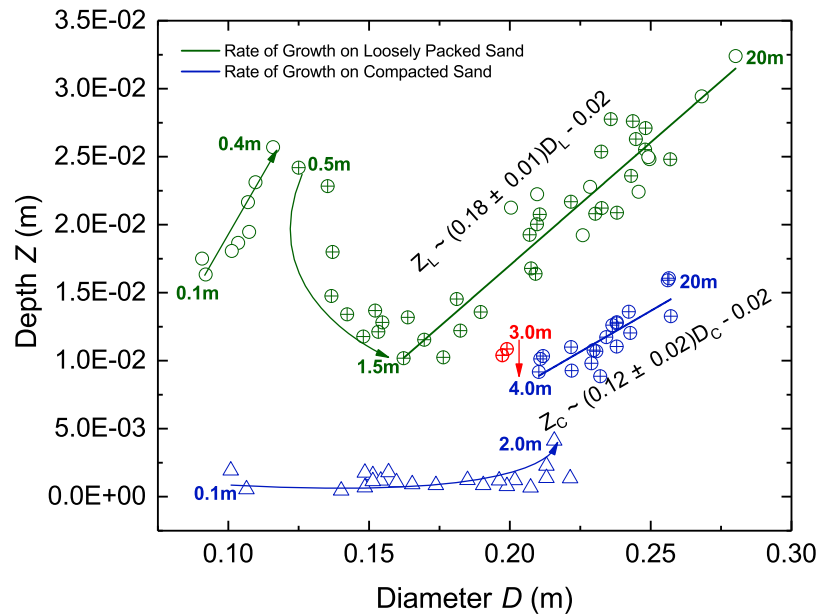
Fig. 3.10 The rate of change of depth with respect to diameter can be observed for both loosely packed and compacted sand experiments.

The relationship between depth and diameter in Figure 3.10 is characterized by a linear fit. In the case of loosely packed sand, a relationship of $Z_L \sim 0.18 D_L$ is obtained, and for compacted sandbox experiments, $Z_L \sim 0.12 D_L$. Although this may seem like the aspect ratio of this group of craters, and it also coincides with the aspect ratio found in craters with

diameters less than 15 km on planets and asteroids, it is nothing more than the growth rate of depth with respect to diameter.

To conduct a proper analysis, it is necessary to explore the data statistically. We analyze the depth aspect ratios as a function of the diameter in our experiments and compare them with the aspect ratios of lunar craters obtained through direct observational measurements conducted on more than 300 lunar craters, see Figure 3.11. The purpose of this comparison is to interpret the shallowness of planetary craters in the context of the uniaxial compression mechanism proposed in this study. It is noteworthy that the depth utilized to calculate the aspect ratio aligns with the commonly employed measurement in the astronomical scientific community, extending from the height of the crater rim to the point of maximum depression within, denoted as $d_{\max}$.

The aspect ratio determined in the experiments conducted in the loosely packed sandbox for dropping heights between $0.1 - 0.4$ m (red distribution in Figure 3.11b $Z_{\mathrm{L}} = (0.193 \pm 0.016)D_{\mathrm{L}}$) closely aligns with the aspect ratio observed in lunar craters with diameters below 15 km (red distribution to the right in Figure 3.11a). This particular aspect ratio corresponds to simple craters—bowl-shaped depressions with raised rims and approximately parabolic interior profiles—with diameters smaller than 15 km, exemplified by the Lunar crater Kepler C [65]. Additionally, during the OSIRIS-REx spacecraft's mission to the asteroid Bennu in 2020, craters of a few meters in diameter were discovered with aspect ratios ranging between 0.1 and 0.2 [24].

In contrast, experimentally, for higher impact energies, aspect ratios of $Z_{\mathrm{C}} = (0.051 \pm 0.006)D_{\mathrm{C}}$ and $Z_{\mathrm{L}} = (0.094 \pm 0.015)D_{\mathrm{L}}$ are observed (blue and green distributions in Figure 3.11b). These align with many of the aspect ratios of lunar craters with diameters between 15 and 100 km, as evident in the blue-green distribution in Figure 3.11a. This category includes lunar craters with flat interiors and larger diameters, such as crater Autolycus [63] and crater Euler J [64].

Some current models, based on scaling equations rather than direct observational values, provide theoretical values that approximate these results. For instance, Pike in 1974 [85] reported a coefficient of 0.196 for craters on the Moon with diameters less than 15 km. Similarly, the lunar impact crater database [55] offers theoretical values from current models; analyzing their data yields aspect ratios of $Z \sim 0.2D$ for diameters less than 15 km and $Z \sim 0.07D$ for diameters between $15 - 100$ km. The striking similarity between observational and experimental aspect ratios deepens our insight into the planarity of lunar craters, allowing us to interpret it through the proposed uniaxial compression model. This contribution significantly advances our understanding of crater morphogenesis. Therefore, it is important to have updated databases that consider direct observational values.
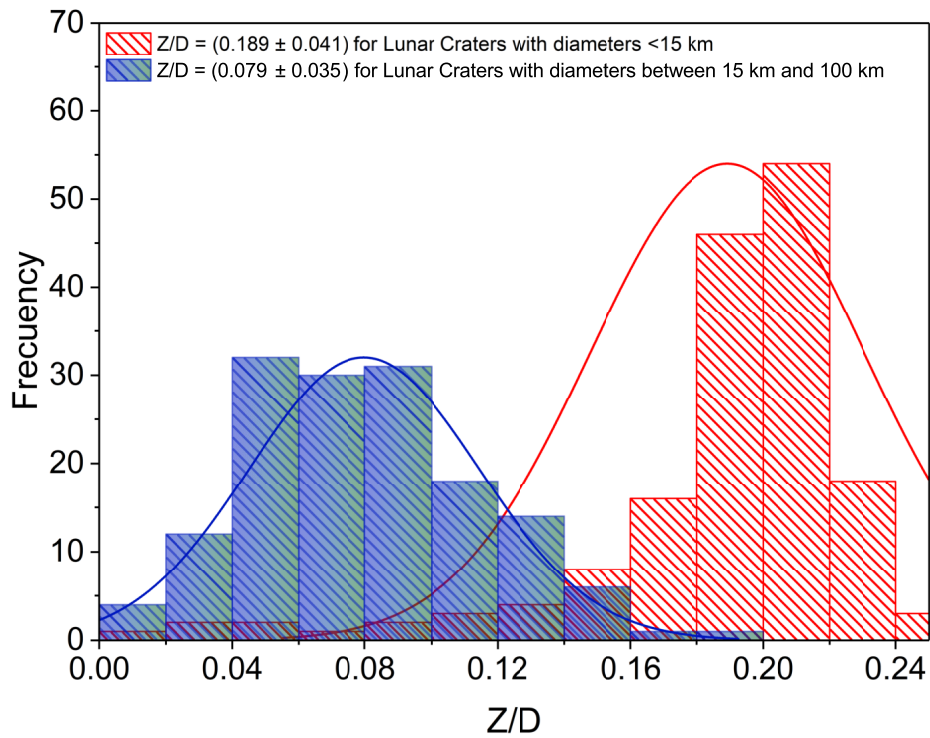
(a)
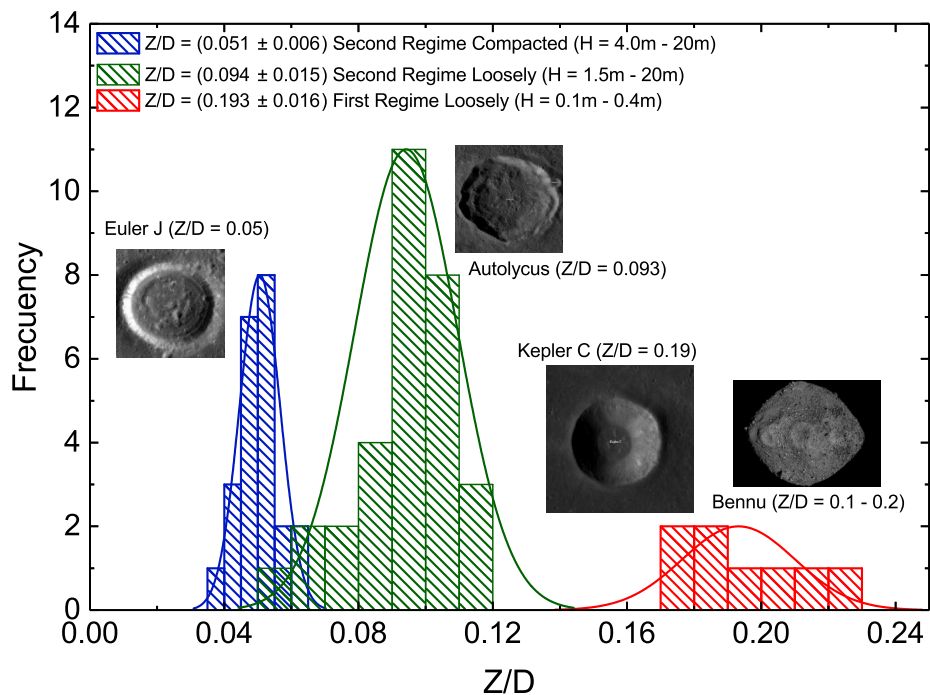
(b)

Fig. 3.11 Aspect ratio between diameter and depth. (a) This figure illustrates aspect ratios directly measured from observational values. The blue-green distribution corresponds to craters with diameters between 15 - 100 km, while the second red distribution represents the aspect ratio for craters with diameters below 15 km. (b) Experimental aspect ratios for both loosely packed and compacted sandbox scenarios. The initial blue distribution corresponds to dropping heights of 4.0 - 20 m in the compacted sandbox. The subsequent green and red distributions correspond to the loosely packed sandbox for dropping heights of 1.5 - 20 m and 0.1 - 0.4 m, respectively.

3.2.3   Volumes

The *craterslab* library offers the advantage of directly calculating crater volumes in a numerical manner, thereby eliminating the need for geometric approximations. These volumes, described as observables in Section 2.2, include, for example, the interior volume of the crater cavity from the rim to its maximum depression (Cavity Volume, V_{in}), and the volume inside the crater below the impact surface origin (Excavated Volume, V_{ex}). Let's conduct a quick morphometric exploration on them.
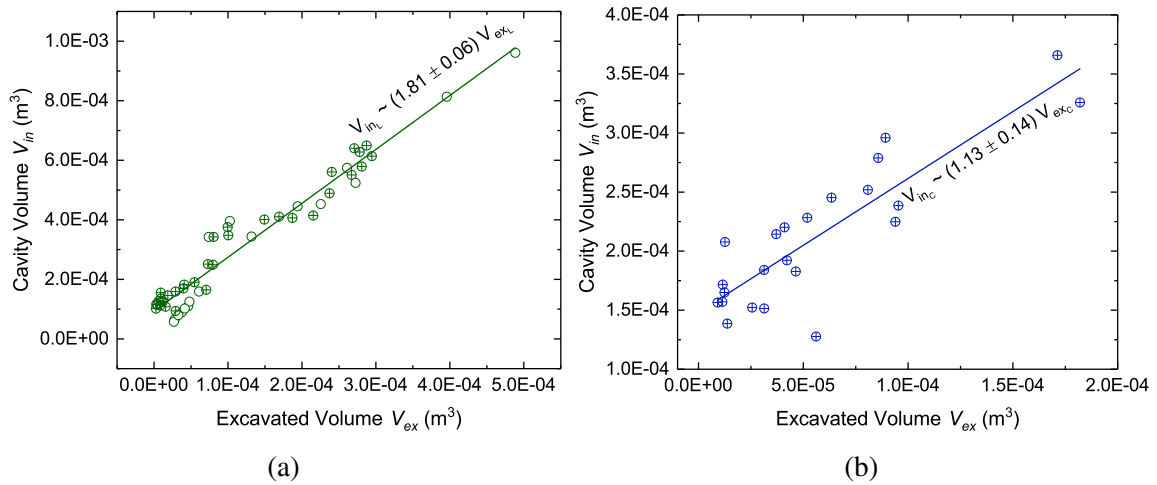

Fig. 3.12 The relationship between cavity and excavated volumes exhibits a linear dependency for both loosely packed sand (a) and compacted sand (b).

The relationship between cavity and excavated volumes exhibits a linear dependency for both loosely packed sand (Figure 3.12a) and compacted sand (Figure 3.12b). This linear dependency arises because the cavity volume inherently contains the excavated volume in both experimental cases. Consequently, we will focus our study on the crater cavity volume. It's important to note that the data in Figure 3.12b represent the second depth regime, where the excavation of impacts begins in compacted sandbox experiments.

Previously, Figure 3.6 explored the energy balance with a focus on a phenomenological analysis using the crater cavity volume. In contrast, Figure 3.13 centers on a morphological analysis of impact craters that can be compared with observational databases, providing insights into the mechanisms involved in the formation process.

The inset of Figure 3.13a illustrates a power-law dependence between the crater cavity volume and its diameter. It confirms that for impacts on loosely packed sandbox, the craters tend to be more spherical, following the relationship $V_{inL} \sim D_L{}^{3.5}$. Conversely, for impacts on compacted sandbox, a relationship of $V_{inC} \sim D_C{}^{2.64}$ holds, indicating less spherical shapes. Interestingly, Nahmad *et al.* [10], employing geometric approximations ($V_{in} \sim D^2Z$), obtain

a power-law relationship with an approximate coefficient of ~ 2.50. This coherence is understandable since these geometric approximations were applied to lunar craters with very low aspect ratios, resembling craters in compacted sandbox experiments. However, direct measurements of the volumes of planetary craters using the *craterslab* library would be beneficial for comparative purposes with experimental impact crater volumes measured using the same technique.
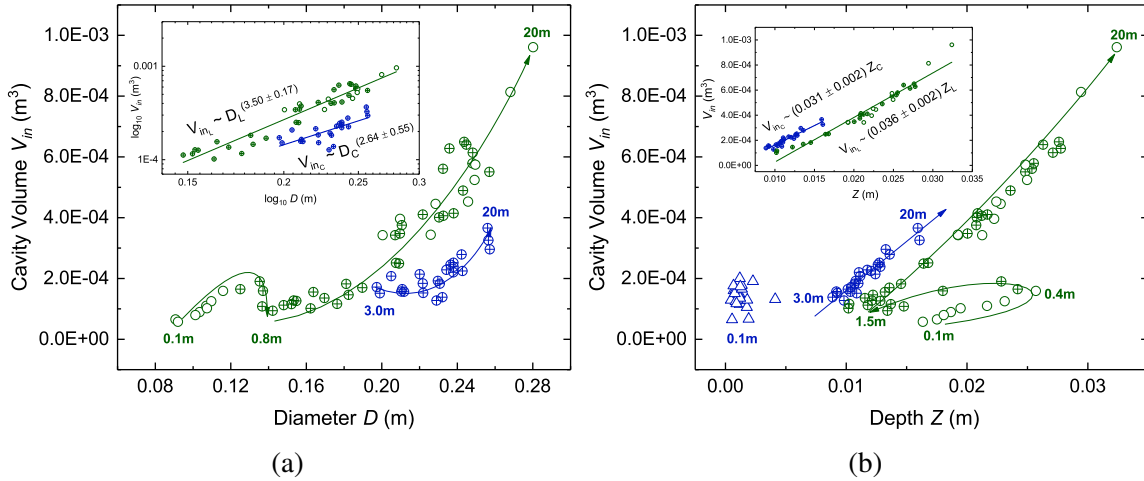

Fig. 3.13 Dependence of cavity volume on diameter and depth for loosely packed and compacted sandbox experiments in the second depth regime. Arrows are used in the figures as a visual guide to understand the transitions between regimes. (a) Regarding diameter, both cases exhibit a power-law dependence. (b) Meanwhile, for depth, they show a linear dependence.

On the other hand, the inset of Figure 3.13b demonstrates a linear dependence ($V_{\text{in}} \sim 0.03Z$) between the crater cavity volume and its depth d_{max} in both experimental groups. However, it's notable in this figure that the cavity volume of craters in compacted sandbox appears to be higher, at least within a certain range, than that of experiments in loosely packed sandbox. This discrepancy arises from an energetic shift in the data. The explanation is that while volumes in compacted sandbox experiments are formed at a 3.0 m drop height with only half the impact energy, loosely packed sand experiments already approach these volumes at a 1.5 m drop height.

3.2.4   A New Paradox

Next, we will analyze the excess volume V_{exc}. This volume represents the volume of the crater lips plus the scattered remains of impactors over the impact surface origin. Experiments conducted on compacted sand have the peculiarity of forming sand mounds in almost half of

the experimental data, with the other half containing scattered remains of the impactor on the surface after impacts. This affects the measurements of the excess volume in compacted sand experiments, leaving few data points for statistical consideration. However, these data points are still interesting and will be discussed as specific cases. Therefore, we will primarily focus on loosely packed sand data for the analysis.

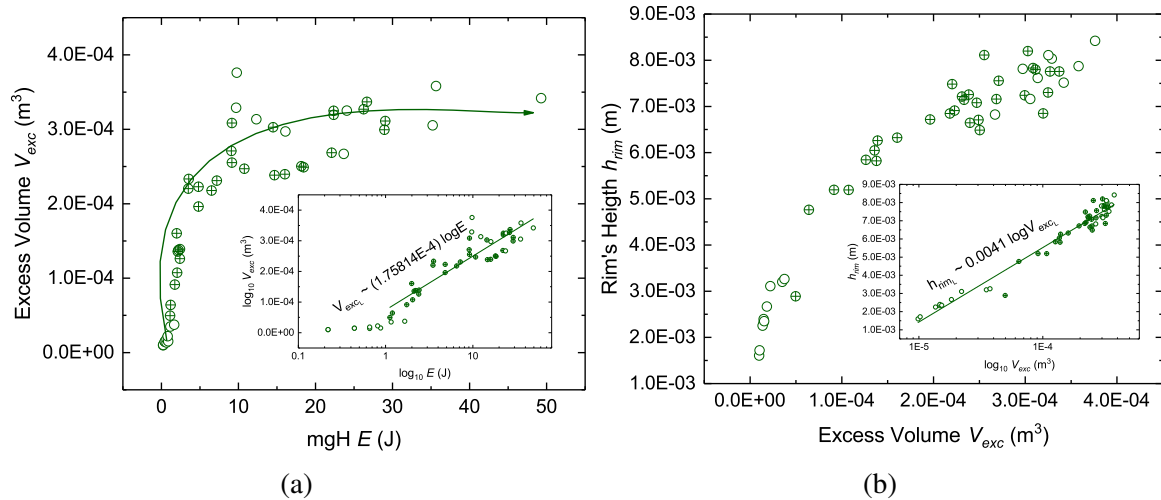(a)   (b)

Fig. 3.14 Dependence of excess volume on impact energy and its growth rate concerning rim height. Arrows are used in the figure (a) as a visual guide. (a) This figure illustrates the saturation of the volume of crater lips. The inset of this figure shows saturation that follows a logarithmic dependence on energy. (b) The inset of this figure shows a logarithmic relationship between the rim height and the volume of the crater lips. This provides the notion of slow growth in rim height concerning this volume.

Figure 3.14a illustrates a logarithmic growth of the excess volume concerning the impact energy. This volume can be considered as the volume of the crater lips from a drop height of $0.6\,\mathrm{m}$ (the point where they begin to form, as observed in Figure 3.1a) plus the fraction of the remains of the impactors, representing less than $1/20$ of the projectile diameter.

The logarithmic dependence found in the inset of Figure 3.14a provides insight into the slow growth of the volume of the crater lips as the impact energy increases. However, this volume has a direct relationship with the average height of the crater lips (h_{rim}); let's explore this observable. Interestingly, Figure 3.14b also shows a logarithmic relationship between the average height of the crater rim and its volume. This result seems to indicate that the volume of the lips increases insignificantly in the Z axis direction. Currently, we are unaware of the dependence that governs the lateral growth of the volume of the lips.

The logarithmic dependence between excess volume and impact energy, along with its logarithmic growth rate in the vertical direction, is intriguing. From these results, establishing a mathematical relationship between rim height and impact energy yields $h_{\mathrm{rim}} \propto \log(\log E)$.

This relationship is experimentally verified, as depicted in the inset of Figure 3.15, highlighting the abrupt saturation of rim height.
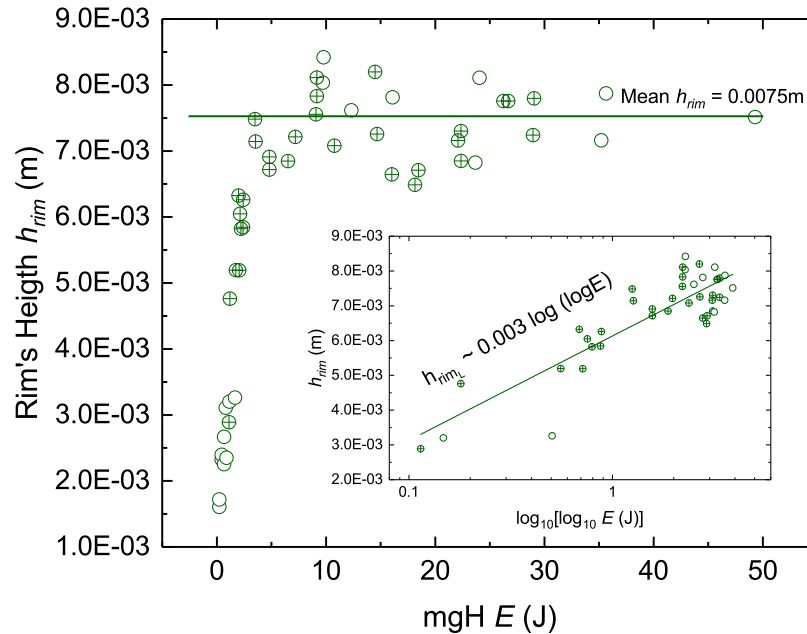

Fig. 3.15 Dependence of the rim height on impact energy. A double logarithmic dependence is shown between the rim height and impact energy, leading to rim height saturation and a new paradox. Arrow is used in the figure as a visual guide.

A valid assumption is that as the impact energy increases, the rim height of the craters will also increase; however, counterintuitively, it saturates. This double logarithmic dependence allows it to grow so slowly that it leads to a saturation event. But how can we verify that this phenomenological analysis is correct? To answer this question, we conducted a comparative analysis between lunar craters and our experiments from a morphometric perspective, as shown in Figure 3.16.

This figure illustrates the gradual increase in rim height relative to diameter with a logarithmic dependence, showcasing rim height saturation between dropping heights of 1.5 m to 20 m in loosely packed sand experiments. A similar trend is observed in compacted sand experiments between dropping heights of 3.0 m and 20 m. As a comparative analysis, we utilize direct observational measurements by our group and theoretical data based on scaling laws [45, 86] from the lunar impact crater database [55], see Figure 3.16b. Despite employing different methods for morphological measurements, in both cases, we observe that the rim height does not exceed 2.5 km. Finally, the experimentally determined logarithmic dependence identified in Figure 3.16a is validated in lunar craters through direct measurements, as depicted in the inset of Figure 3.16b.
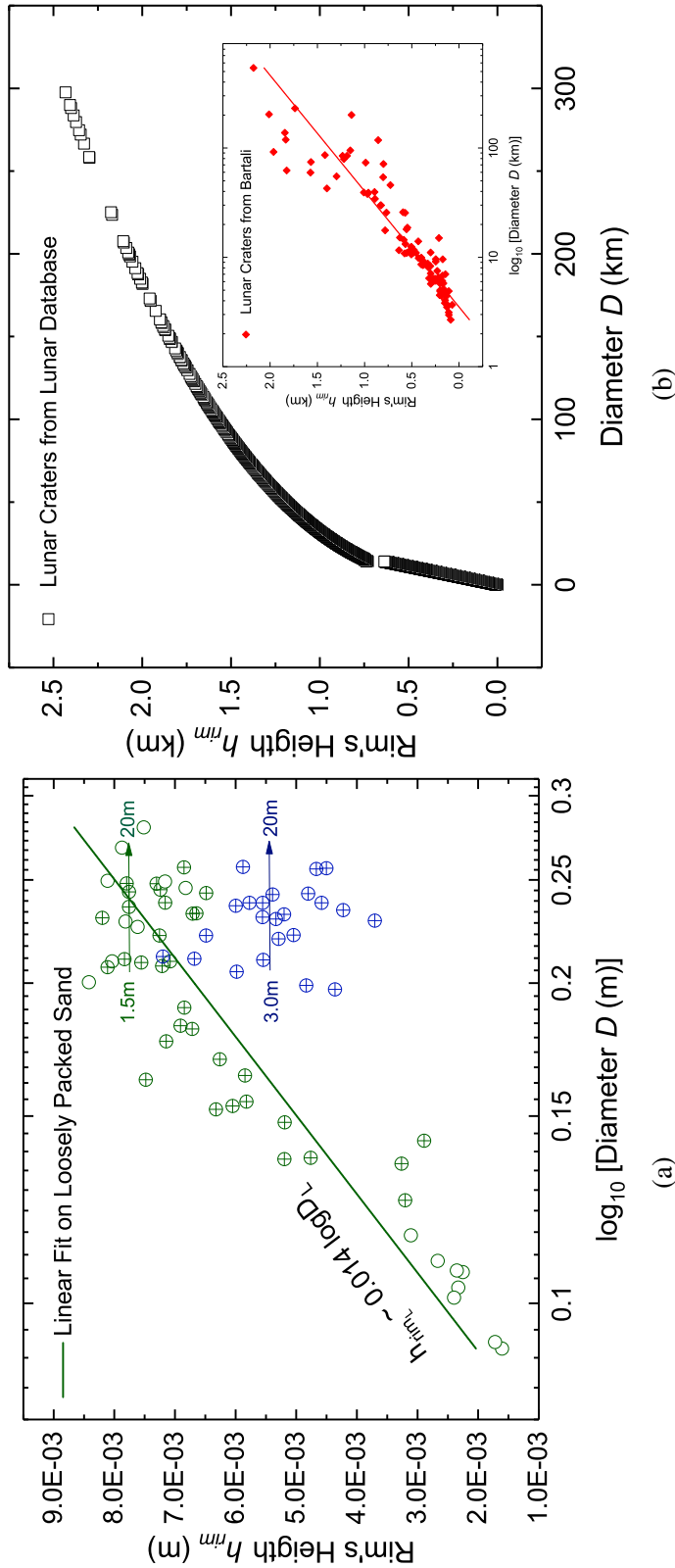
Fig. 3.16 This figure illustrates the morphometric comparison conducted between the dependencies of rim height and crater diameter in both experimental and direct observational analyses of lunar craters. (a) The data from loosely packed and compacted sand are shown. The first set (green symbols) undergoes a linear fit on the semilog plot, showing a saturation mechanism due to a logarithmic dependence; while the second set (blue symbols) serves as a comparison, also exhibiting confined rim height values and being smaller than those of loosely packed sand. Arrows are used in this figure as a visual guide to understand the saturation of both regimes. (b) Over eight thousand craters, ranging in diameter from a few meters to 300 km, were scrutinized in the lunar database. The database estimates, based on theoretical approximations, indicate that the rim height of lunar craters does not exceed 2.5 km. The data presented in the inset comprises direct observational measurements by our group, revealing a logarithmic relationship between rim height and crater diameter. Importantly, these measurements consistently demonstrate that the rim height does not surpass 2.5 km even in craters with diameters of up to 500 km. These direct measurements serve as a correction to prevailing theoretical models.

In light of these experimental results, validated through observations, a new paradox emerges that, to the best of our knowledge, has not yet been addressed. Despite the Moon not being subject to tectonic plate movements that could drive the growth of mountain ranges and having lower gravity compared to Earth, Mars, and Mercury, Mons Huygens [60] stands as the tallest mountain with approximately $\sim 5\,\text{km}$ in height. Nevertheless, the extremely energetic impact that formed it should have created a mountain possibly exceeding $\sim 30\,\text{km}$ in height. The heights of these mountains should be governed by their weight according to gravity, suggesting kilometer-scale heights. However, the majority does not exceed 2.5 km in height, as observed in Figure 3.16b. This intriguing contradiction prompts us to delve deeper into the underlying mechanisms governing the morphological features of lunar craters and the apparent limitation in rim height. Meanwhile, we can reflect on the following paradox:

"Why does the rim height of lunar craters saturate at just a few kilometers when, in the presence of such violent energetic impacts and at such low gravity, it should be much higher than on Mars, Earth, and Mercury?"

3.2.5   Lateral Opening Mechanisms

In Subsection 3.2.1, Uehara's model describes how the crater diameter scales with an exponent of $\sim 1/4$ concerning the projectile's impact energy based on a "gravity-limited" regime. Figure 3.9 confirms this theory for impacts on loosely packed sand. However, it is essential to note that, strangely, the exponent changes in the case of compacted sand to $D \propto H^{1/8}$. Based on the morphometric exploration conducted in the previous subsection, let's revisit this topic.

Interestingly, in Figure 3.17, V_{exc} exhibits a linear dependence on the diameter with a coefficient of relation of 0.00197, which is very low. Now, let's consider the dependencies obtained in Figures 3.17 and 3.14a and establish a mathematical relationship between them. The logarithmic growth in Figure 3.14a can be expressed as $V_{exc} \sim (1.75814 \times 10^{-4}) \log E$, and according to Figure 3.17, it holds that $V_{exc} \sim 0.00197 D_{L}$.
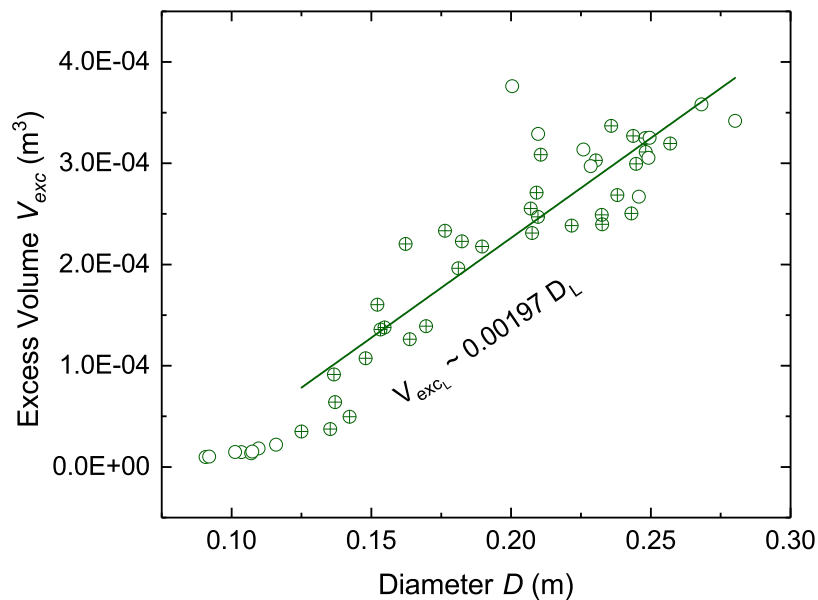
Fig. 3.17 The excess volume follows a linear relationship, with a very small coefficient (0.00197), with respect to the diameter.

By expressing the relationship between the diameter and the energy based on the previous dependencies, we obtain Equation 3.10, which is experimentally confirmed, see Figure 3.18. This new result prompts us to question the "gravity-limited" regime model proposed by Uehara et al. [109] and reconsider the mechanisms involved in the lateral opening of craters.

$$D_{\mathrm{L}} \sim 0.089 \log E \qquad (3.10)$$

Fig. 3.18 New logarithmic growth dependency of the diameter on impact energy with a relation $D_{\mathrm{L}} \sim 0.083 \log E$, close to the mathematical approximation of Equation 3.10. In the case of compacted sandbox, which previously strangely fit with an exponent of $\sim 1/8$, a similar logarithmic growth to loosely packed sand experiments is observed. In order to establish a correct lateral opening mechanism, we use data that surpasses the critical energy that allows excavation on the impact surface allowing the formation of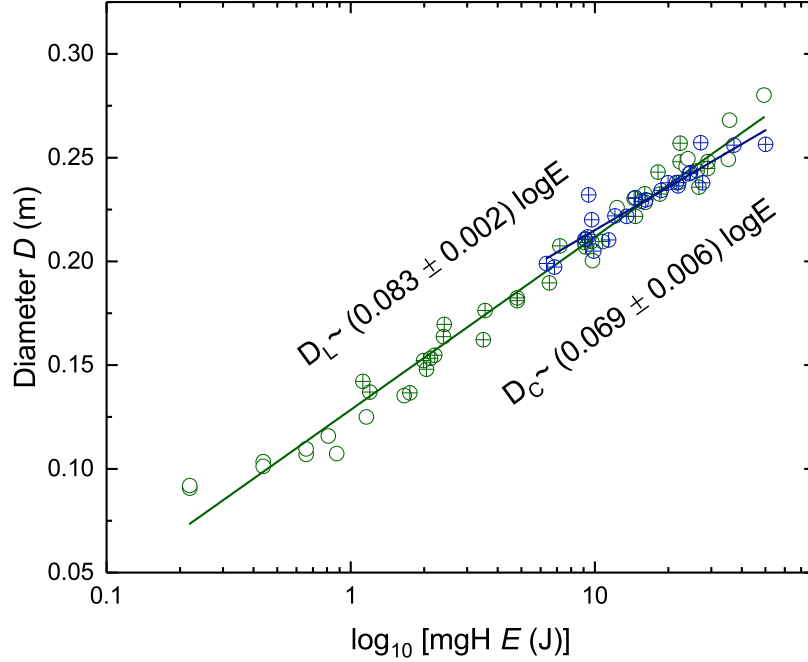 craters (the second regime). In this case, a similar numerical approximation like Equation 3.10 is not carried out due to insufficient data.

To address Equation 3.10, we propose a radial opening model, considering that the majority of planetary craters exhibit a cylindrical geometry, which remains an open question in the scientific community.

The principle of energy conservation dictates that the net work done on an object equals the change in its kinetic energy, expressed as $\Delta W = \Delta E_{\mathrm{K}}$. This relationship can be applied to the lateral opening mechanism of a crater, assuming a cylindrical geometry where the dynamic force of crater opening F_{dl} is uniformly distributed radially in all directions. Equation 3.11 formalizes this mechanism:

$$F_{\mathrm{dl}} \cdot \mathrm{d}r = \Delta E_{\mathrm{l}} = \alpha \Delta E_{\mathrm{v}} = \alpha \frac{1}{2} m_{\mathrm{p}} \cdot \mathrm{d}V_{\mathrm{p}}^{2} \qquad (3.11)$$

Here, m_p and V_p represent the mass and vertical impact velocity of the projectile, respectively, while α represents the fraction of lateral energy change relative to the vertical energy of the projectile.

Considering the lateral dynamic force as a fraction (β) of the vertical dynamic force ($F_{dl} = \beta F_{dv}$), Equation 3.11 becomes:

$$\beta \rho_p \cdot A_p \cdot dr = \alpha m_p \cdot \frac{dE}{E} \tag{3.12}$$

Here, ρ_p and A_p represent the density and cross-sectional area of the projectile, respectively, while E represents the impact energy.

Integrating both sides of Equation 3.12 yields the logarithmic relationship:

$$\beta \rho_p \cdot A_p \cdot D + C_1 \propto \alpha m_p \cdot \log E + C_2 \tag{3.13}$$

In this equation, D represents the diameter of the crater, and C_1 and C_2 are constants.

This model proposes a lateral opening mechanism based on cylindrical geometry grounded in the principle of energy conservation. It establishes a logarithmic dependence of the form $D \propto \log E$ for both loosely packed and compacted sandbox experiments. The lateral area of the crater, in relation to the excavation depth ($A_c \propto d_{exc}$), is considered instead of the depth (d_{max}), which encompasses the crater's rim height. This adjustment is made because, experimentally, a significant uplift mechanism has not been directly observed. Instead, the predominant lateral mechanism is attributed to granular bulldozing [100, 99]. Consequently, the crater lips primarily result from folds formed by different shear layers beneath the impact surface [20, 123, 95]. Relevant examples can be found in a set of images from two-dimensional experiments [9].

From an energetic standpoint, it is logically inferred that the kinetic energy of the impact transforms into lateral kinetic energy. A portion of this energy contributes to the opening of the crater while dissipating due to the effective friction among the sand grains in the lateral area. Simultaneously, another portion transforms into kinetic energy, propelling the projectile debris. The remaining fraction of vertical kinetic energy converts into heat due to friction in the compaction mechanism. Consequently, based on this model, it can be posited that the impact energy undergoes transformation in such a manner that the residual lateral energy dissipates as the crater diameter increases. This results in a gradual expansion of the crater diameter, aligning with the observed logarithmic relationship in Equation 3.10 and Figure 3.18.

Chapter 4

Conclusions

In summary, we experimentally generated impact craters in granular terrain by varying both energy and surface compaction. We introduced a novel methodology for impact crater studies using Time-of-Flight (ToF) sensors, specifically the KinectToF camera, and validated our approach by comparing it with the established profilometry technique. The topographic data obtained through KinectToF, considering different impacting energies and compaction levels of the target terrain, revealed diverse crater shapes. We automated the measurement of key morphological features, including shape, depth, diameter, local slope, excess and excavated volumes, as well as cavity volume and rim height. KinectToF exhibited high precision, surpassing the performance of laser profilometry.

As part of this thesis, we introduce the software *craterslab*, designed for the acquisition of data and morphological analysis of experimental and planetary impact craters. *Craterslab*, when combined with LiDAR sensors, delivers highly accurate results for crater morphology, reducing the time required for data acquisition and analysis compared to previous methods. Furthermore, it enables the direct numerical calculation of certain morphological characteristics with great precision, such as cavity volume, which was previously only obtained through geometric approximations. The automated generation of a three-dimensional map along with a comprehensive set of morphometric features provided by the library opens the door to detailed exploration, potentially leading to new analyses and theories. This library stands among the first to be available in the scientific community for topographic analyses of craters. Utilizing this innovative technique, we can provide a detailed description of the morphology and formation mechanisms of impact craters. The implications of this study extend beyond laboratory experiments, facilitating the exploration of features in planetary craters that were previously not well understood; *craterslab* represents a significant advancement in the systematic analysis of impact craters, offering a more accurate and efficient approach to understanding both laboratory-scale experiments and planetary features.

From the morphological exploration conducted in our experimental setup, certain inconsistencies with results reported in the literature were identified. The plastic deformation-based model that governs the behavior of crater interior depth does not provide a satisfactory fit in either case. To overcome this limitation, we introduce a uniaxial compaction model with an exponential law, explaining how depth saturates to a filling fraction equal to random close packing. This model clarifies the underlying physical mechanisms of vertical compression, lateral excavation of the crater, and the transfer of momentum between these degrees of freedom. Our findings suggest that planetary craters are more likely formed by granular impacts on granular surfaces, emphasizing the crucial importance of understanding crater-opening mechanisms in such collisions. Hence, the proposed model serves as a novel theoretical tool for addressing this longstanding problem. Within this energy balance framework, frictional forces play a pivotal but not yet fully revealed role. Our results highlight a greater transfer of vertical to horizontal momentum on compacted surfaces compared to loosely packed sandbox targets, with central peak formation emerging as a critical process, representing a possible mechanism of momentum transfer from vertical to horizontal degrees of freedom.

On another note, the power-law relationship governing crater diameters seems to exhibit consistency with a volume-displacement model for experiments conducted on loosely packed sand. Meanwhile, a more favorable fit with an exponent of approximately $\sim 1/8$ was obtained for the compacted sandbox target. This latter result drew our attention to the physical processes that should be involved in the lateral opening mechanism, leading us to develop a cylindrical opening model. This model, based on the principle of energy conservation, corroborates the experimentally obtained dependence of $D \propto \log E$ for both loosely packed and compacted sandbox. The energy analysis considered in this model and complementary experimental observations suggest that the predominant lateral mechanism involves granular bulldozing, with crater lips formed by folds resulting from various shear layers beneath the impact surface, instead of solely considering the uplift mechanism in the current model.

On the contrary, the models proposed based on a "gravity-limited" regime ($D \propto E^{1/4}$) and plastic deformation ($Z \propto E^{1/3}$) present power laws that resemble slow growth rates for diameter and depth but do not provide answers to the physical mechanisms present in crater formation processes. While acknowledging the limitations, it is crucial to recognize the significance of these models as pioneering contributions that initiated investigations in this field and laid the foundation for our subsequent research. The evolving understanding gained from these early models has informed and guided our current exploration of crater formation mechanisms.

Moreover, the morphometric analysis conducted revealed remarkably similar aspect ratios between experimental and planetary craters. The aspect ratio obtained in the first depth regime of loosely packed sand ($Z \sim 0.193D$) corresponds to simple craters with diameters smaller than 15 km, displaying bowl-shaped depressions and raised rims. This aspect ratio aligns with previous observations on the Moon and asteroids. In the second regime, representing craters with flat interiors and larger diameters, the aspect ratios ($Z \sim 0.094D$ for loosely packed sand and $Z \sim 0.051D$ for compacted sand) coincide with those of planetary craters, particularly lunar craters, where aspect ratios between 0.05 and 0.09 has been observed in the diameter range of 15 to 100 km. These comparative findings contribute significantly to advancing our understanding of crater morphogenesis.

Finally, in a wholly counterintuitive manner, the analysis of crater lip volume reveals an abrupt saturation of rim height concerning impact energy, governed by a double logarithmic law. When exploring the morphometrics of lunar craters in terms of rim height and diameter, a simple logarithmic dependence emerges, leading to saturation and subsequently validated through experimentation. In light of these counterintuitive findings on lunar crater rim heights, the analysis of crater lip volume and the observed logarithmic dependence in morphometric exploration prompt a deeper investigation into the underlying mechanisms, setting the stage for the paradoxical nature of lunar geological features. Despite the Moon lacking tectonic plate movements and having lower gravity than Earth, Mars, and Mercury, Mons Huygens stands as the tallest mountain at ~ 5,km, formed by an impact that should have resulted in a height of ~ 30,km. However, the observed heights of lunar mountains in the database and from direct measurements do not exceed 2.5 km, presenting a paradox:

"Why does the rim height of lunar craters saturate at just a few kilometers, given the violent impacts and low gravity, when it should be much higher than on Mars, Earth, and Mercury?"

References

[1] Alvarez, L. W., Alvarez, W., Asaro, F., and Michel, H. V. (1980). Extraterrestrial cause for the cretaceous-tertiary extinction. *Science*, 208(4448):1095–1108.

[2] Alvarez, W., Claeys, P., and Kieffer, S. W. (1995). Emplacement of cretaceous-tertiary boundary shocked quartz from chicxulub crater. *Science*, 269(5226):930–935.

[3] Amarouchene, Y., Boudet, J., and Kellay, H. (2001). Dynamic sand dunes. *Physical review letters*, 86(19):4286.

[4] Amato, J. C. and Williams, R. E. (1998). Crater formation in the laboratory: An introductory experiment in error analysis. *American Journal of Physics*, 66(2):141–143.

[5] Ambroso, M., Santore, C., Abate, A., and Durian, D. J. (2005). Penetration depth for shallow impact cratering. *Physical Review E*, 71(5):051305.

[6] Anderson, L. and Wood, C. (1978). New morphometric data for fresh lunar craters.

[7] Andreotti, B., Forterre, Y., and Pouliquen, O. (2013). *Granular media: between fluid and solid*. Cambridge University Press, New York.

[8] Asphaug, E., Ryan, E. V., and Zuber, M. T. (2002). Asteroid interiors. *Asteroids III*, 1:463–484.

[9] Bartali, R., Nahmad-Molinari, Y., and Rodríguez-Liñán, G. M. (2015). Low speed granular–granular impact crater opening mechanism in 2d experiments. *Earth, Moon, and Planets*, 116:115–138.

[10] Bartali, R., Rodríguez-Liñán, G. M., Nahmad-Molinari, Y., Sarocchi, D., and Ruiz-Suárez, J. C. (2013). Role of the granular nature of meteoritic projectiles in impact crater morphogenesis.

[11] Borg, J., Morrissey, M., Perich, C., Vogler, T., and Chhabildas, L. (2013). In situ velocity and stress characterization of a projectile penetrating a sand target: Experimental measurements and continuum simulations. *International Journal of Impact Engineering*, 51:23–35.

[12] Bray, V. J., Collins, G. S., Morgan, J. V., and Schenk, P. M. (2008). The effect of target properties on crater morphology: Comparison of central peak craters on the moon and ganymede. *Meteoritics & Planetary Science*, 43(12):1979–1992.

[13] Buckingham, E. (1914). On physically similar systems; illustrations of the use of dimensional equations. *Physical review*, 4(4):345.

[14] Carbone, V., Carocci, M., Savio, E., Sansoni, G., and De Chiffre, L. (2001). Combination of a vision system and a coordinate measuring machine for the reverse engineering of freeform surfaces. *The International Journal of Advanced Manufacturing Technology*, 17:263–271.

[15] Cárdenas-Barrantes, M., Cantor, D., Barés, J., Renouf, M., and Azéma, E. (2021). Micromechanical description of the compaction of soft pentagon assemblies. *Physical Review E*, 103(6):062902.

[16] Center, M. E. (2023). High-speed photography techniques. https://edgerton.mit.edu/.

[17] Chappelow, J. (2013). Simple impact crater shape determination from shadows. *Meteoritics & Planetary Science*, 48(10):1863–1872.

[18] Chauhan, P., Kaur, P., Srivastava, N., Bhattacharya, S., Ajai, Kumar, A. K., and Goswami, J. (2012). Compositional and morphological analysis of high resolution remote sensing data over central peak of tycho crater on the moon: implications for understanding lunar interior. *Current Science*, pages 1041–1046.

[19] Chávez, G. M., Sarocchi, D., Santana, E. A., Borselli, L., and Rodríguez-Sedano, L. (2014). Using kinect to analyze pebble to block-sized clasts in sedimentology. *Computers & Geosciences*, 72:18–32.

[20] Ciamarra, M. P., Coniglio, A., and Nicodemi, M. (2005). Shear instabilities in granular mixtures. *Physical review letters*, 94(18):188001.

[21] Collins, G. S., Melosh, H. J., and Marcus, R. A. (2005). Earth impact effects program: A web-based computer program for calculating the regional environmental consequences of a meteoroid impact on earth. *Meteoritics & planetary science*, 40(6):817–840.

[22] Corrales-Machín, F., Nahmad-Molinari, Y., Viera-López, G., and Bartali, R. (2023a). Crater depth prediction in granular collisions: A uniaxial compression model. *arXiv preprint arXiv:2311.00898*.

[23] Corrales-Machín, F., Viera-López, G., Bartali, R., and Nahmad-Molinari, Y. (2023b). Morphological study of granular-granular impact craters through time-of-flight cameras: from concept to automation in python. *arXiv preprint arXiv:2310.13834*.

[24] Daly, R. T., Barnouin, O. S., Bierhaus, E. B., Daly, M. G., Seabrook, J. A., Ballouz, R. L., Nair, H., Espiritu, R. C., Jawin, E. R., Trang, D., et al. (2022). The morphometry of small impact craters on bennu: Relationships to geologic units, boulders, and impact armoring. *Icarus*, 384:115058.

[25] Davis, C. H. (1992). Satellite radar altimetry. *IEEE transactions on microwave theory and techniques*, 40(6):1070–1076.

[26] Davison, T. M., Ciesla, F. J., and Collins, G. S. (2012). Post-impact thermal evolution of porous planetesimals. *Geochimica et Cosmochimica Acta*, 95:252–269.

[27] De Vet, S. J. and de Bruyn, J. R. (2007). Shape of impact craters in granular media. *Physical Review E*, 76(4):041306.

[28] Dong, P. and Chen, Q. (2017). *LiDAR remote sensing and applications*. CRC Press, FL.

[29] Duran, J. (2012). *Sands, powders, and grains: an introduction to the physics of granular materials*. Springer Science & Business Media.

[30] Efford, N. D. (1991). Sources of error in the photoclinometric determination of planetary topography: A reappraisal. *Earth, Moon, and Planets*, 54(1):19–58.

[31] El-laithy, R. A., Huang, J., and Yeh, M. (2012). Study on the use of microsoft kinect for robotics applications. In *Proceedings of the 2012 IEEE/ION Position, Location and Navigation Symposium*, pages 1280–1288. IEEE.

[32] Erick Malaret (1988). Applied coherent technology (act) corporation, for sensor data capture and management through analysis. https://www.actgate.com/about.

[33] Essmaeel, K., Gallo, L., Damiani, E., De Pietro, G., and Dipanda, A. (2012). Temporal denoising of kinect depth data. In *2012 Eighth International Conference on Signal Image Technology and Internet Based Systems*, pages 47–52. IEEE.

[34] Fujiwara, A., Kawaguchi, J., Yeomans, D., Abe, M., Mukai, T., Okada, T., Saito, J., Yano, H., Yoshikawa, M., Scheeres, D., et al. (2006). The rubble-pile asteroid itokawa as observed by hayabusa. *Science*, 312(5778):1330–1334.

[35] Geng, J. (2011). Structured-light 3d surface imaging: a tutorial. *Advances in Optics and Photonics*, 3(2):128–160.

[36] Giese, B., Oberst, J., Roatsch, T., Neukum, G., Head, J., and Pappalardo, R. (1998). The local topography of uruk sulcus and galileo regio obtained from stereo images. *Icarus*, 135(1):303–316.

[37] Gilbert, G. K. (1979). The moon's face: a study of the origin of its features. In *A Source Book in Astronomy and Astrophysics, 1900–1975*, pages 80–87. Harvard University Press.

[38] González-Gutiérrez, J., Carrillo-Estrada, J., and Ruiz-Suarez, J. (2014). Penetration of granular projectiles into a water target. *Scientific reports*, 4(1):1–5.

[39] Graebling, P., Lallement, A., Zhou, D.-Y., and Hirsch, E. (2002). Optical high-precision three-dimensional vision-based quality control of manufactured parts by use of synthetic images and knowledge for image-data evaluation and interpretation. *Applied Optics*, 41(14):2627–2643.

[40] Hajialilue-Bonab, M. and Rezaei, A. (2009). Physical modelling of low-energy dynamic compaction. *International Journal of Physical Modelling in Geotechnics*, 9(3):21–32.

[41] Heckel, R. (1961). Density-pressure relationships in powder compaction. *Trans. Metal. Soc. AIME*, 221:671–675.

[42] Holsapple, K., Giblin, I., Housen, K., Nakamura, A., and Ryan, E. (2002). Asteroid impacts: Laboratory experiments and scaling laws. *Asteroids III*, 1:443–462.

[43] Holsapple, K. A. (1993). The scaling of impact processes in planetary sciences. *Annual review of earth and planetary sciences*, 21(1):333–373.

[44] Home, R. W. (1972). The origin of the lunar craters: an eighteenth-century view. *Journal for the History of Astronomy*, 3(1):1–10.

[45] Hörz, F., Grieve, R., Heiken, G., Spudis, P., and Binder, A. (1991). Lunar surface processes. *Lunar sourcebook, a user's guide to the Moon*, pages 61–120.

[46] Housen, K. R. and Holsapple, K. A. (2003). Impact cratering on porous asteroids. *Icarus*, 163(1):102–119.

[47] Inglezakis, V. (2016). Extraterrestrial environment. In *Environment and Development*, pages 453–498. Elsevier.

[48] James (1953). Historia de la física: hasta mediados del siglo xx. Technical report.

[49] Jankowski, D. G. and Squyres, S. W. (1991). Sources of error in planetary photoclinometry. *Journal of Geophysical Research: Planets*, 96(E4):20907–20922.

[50] Kadambi, A., Bhandari, A., and Raskar, R. (2014). 3d depth cameras in vision: Benefits and limitations of the hardware: With an emphasis on the first-and second-generation kinect models. *Computer vision and machine learning with RGB-D sensors*, pages 3–26.

[51] Katsuragi, H. and Durian, D. J. (2007). Unified force law for granular impact cratering. *Nature physics*, 3(6):420–423.

[52] Keller, M., Lefloch, D., Lambers, M., Izadi, S., Weyrich, T., and Kolb, A. (2013). Real-time 3d reconstruction in dynamic scenes using point-based fusion. In *2013 International Conference on 3D Vision-3DV 2013*, pages 1–8. IEEE.

[53] Klevan, I., Nordström, J., Bauer-Brandl, A., and Alderborn, G. (2009). On the physical interpretation of the initial bending of a shapiro–konopicky–heckel compression profile. *European journal of pharmaceutics and biopharmaceutics*, 71(2):395–401.

[54] Lachat, E., Macher, H., Mittet, M.-A., Landes, T., and Grussenmeyer, P. (2015). First experiences with kinect v2 sensor for close range 3d modelling. *International Archives of the Photogrammetry, Remote Sensing & Spatial Information Sciences*.

[55] Losiak et al., LPI Lunar Exploration Intern Program (2015). Lunar impact crater database. https://www.lpi.usra.edu/lunar/surface/.

[56] Love, S. G., Hörz, F., and Brownlee, D. E. (1993). Target porosity effects in impact cratering and collisional disruption. *Icarus*, 105(1):216–224.

[57] Lu, K. and Wang, W. (2015). A multi-sensor approach for rapid and precise digitization of free-form surface in reverse engineering. *The International Journal of Advanced Manufacturing Technology*, 79:1983–1994.

[58] Lunar QuickMap (2023a). Complex crater king. https://bit.ly/45cpIGL. We acknowledge the use of imagery from Lunar QuickMap(https://quickmap.lroc.asu.edu), a collaboration between NASA, Arizona State University & Applied Coherent Technology Corp.

[59] Lunar QuickMap (2023b). Complex crater tycho. https://bit.ly/3pYhjYh. We acknowledge the use of imagery from Lunar QuickMap(https://quickmap.lroc.asu.edu), a collaboration between NASA, Arizona State University & Applied Coherent Technology Corp.

[60] Lunar QuickMap (2023c). Mons huygens. https://bit.ly/3HiMXVt. We acknowledge the use of imagery from Lunar QuickMap(https://quickmap.lroc.asu.edu), a collaboration between NASA, Arizona State University & Applied Coherent Technology Corp.

[61] Lunar QuickMap (2023d). Simple crater bernoullie c. https://bit.ly/43AL2nK. We acknowledge the use of imagery from Lunar QuickMap(https://quickmap.lroc.asu.edu), a collaboration between NASA, Arizona State University & Applied Coherent Technology Corp.

[62] Lunar QuickMap (2023e). Simple crater steinheil. https://bit.ly/471E5z5. We acknowledge the use of imagery from Lunar QuickMap(https://quickmap.lroc.asu.edu), a collaboration between NASA, Arizona State University & Applied Coherent Technology Corp.

[63] Lunar QuickMap (2024a). Autolycus. https://bit.ly/3Sm6dXp. We acknowledge the use of imagery from Lunar QuickMap(https://quickmap.lroc.asu.edu), a collaboration between NASA, Arizona State University & Applied Coherent Technology Corp.

[64] Lunar QuickMap (2024b). Euler j. https://bit.ly/4bjf0lq. We acknowledge the use of imagery from Lunar QuickMap(https://quickmap.lroc.asu.edu), a collaboration between NASA, Arizona State University & Applied Coherent Technology Corp.

[65] Lunar QuickMap (2024c). Kepler c. https://bit.ly/49h1SeN. We acknowledge the use of imagery from Lunar QuickMap(https://quickmap.lroc.asu.edu), a collaboration between NASA, Arizona State University & Applied Coherent Technology Corp.

[66] Malaret, E. (2024). Applied coherent technology corporation.

[67] Mars QuickMap (2023). Mound formation on mars. https://bit.ly/3Dlg4ph. We acknowledge the use of imagery from Mars QuickMap(https://mars.quickmap.io/), a collaboration between NASA, Arizona State University & Applied Coherent Technology Corp.

[68] Matlab (2024). Camera calibration.

[69] McClay, K. (1996). Recent advances in analogue modelling: uses in section interpretation and validation. *Geological Society, London, Special Publications*, 99(1):201–225.

[70] McDonald, J. and Montgomery, J. (2015). Real-time crater profile analysis: Visualizing high-resolution laser altimetry data sets on the gpu. *SPECIAL PAPER OF THE GEOLOGICAL SOCIETY OF AMERICA*, 518:213–227.

[71] Melosh, H. and Ivanov, B. (1999). Impact crater collapse. *Annual Review of Earth and Planetary Sciences*, 27(1):385–415.

[72] Melosh, H. J. (1989). Impact cratering: A geologic process. *New York: Oxford University Press; Oxford: Clarendon Press*.

[73] Mercury QuickMap (2023). Complex crater debussy. https://bit.ly/3Do9IW7. We acknowledge the use of imagery from Mercury QuickMap(https://messenger.quickmap.io), a collaboration between NASA, JHU/APL & Applied Coherent Technology Corp.

[Michael, Greg and Annex, Andrew and Aye, Michael] Michael, Greg and Annex, Andrew and Aye, Michael. Craterstats. https://github.com/ggmichael/craterstats.

[75] Mousavi Hondori, H. and Khademi, M. (2014). A review on technical and clinical impact of microsoft kinect on physical therapy and rehabilitation. *Journal of medical engineering*, 2014.

[76] Newcombe, R. A., Izadi, S., Hilliges, O., Molyneaux, D., Kim, D., Davison, A. J., Kohi, P., Shotton, J., Hodges, S., and Fitzgibbon, A. (2011). Kinectfusion: Real-time dense surface mapping and tracking. In *2011 10th IEEE international symposium on mixed and augmented reality*, pages 127–136. Ieee.

[77] Nießner, M., Zollhöfer, M., Izadi, S., and Stamminger, M. (2013). Real-time 3d reconstruction at scale using voxel hashing. *ACM Transactions on Graphics (ToG)*, 32(6):1–11.

[78] ORBBEC (2024). Femto bolt.

[79] Osinski, G. R. and Pierazzo, E. (2013). Impact cratering: Processes and products. *Impact Cratering*, pages 1–20.

[80] Ostro, S. J., Margot, J.-L., Benner, L. A., Giorgini, J. D., Scheeres, D. J., Fahnestock, E. G., Broschart, S. B., Bellerose, J., Nolan, M. C., Magri, C., et al. (2006). Radar imaging of binary near-earth asteroid (66391) 1999 kw4. *Science*, 314(5803):1276–1280.

[81] Pacheco-Vázquez, F. (2019). Ray systems and craters generated by the impact of nonspherical projectiles. *Physical review letters*, 122(16):164501.

[82] Pacheco-Vázquez, F. and Ruiz-Suárez, J. (2011). Impact craters in granular media: grains against grains. *Physical review letters*, 107(21):218001.

[83] Pagliari, D. and Pinto, L. (2015). Calibration of kinect for xbox one and comparison between the two generations of microsoft sensors. *Sensors*, 15(11):27569–27589.

[84] Pierazzo, E. and Collins, G. (2004). A brief introduction to hydrocode modeling of impact cratering. In *Cratering in marine environments and on ice*, pages 323–340. Springer.

[85] Pike, R. J. (1974). Craters on earth, moon, and mars: Multivariate classification and mode of origin. *Earth and Planetary Science Letters*, 22(3):245–255.

[86] Pike, R. J. (1976). Crater dimensions from apollo data and supplemental sources. *The Moon*, 15(3-4):463–477.

[87] Pittman, S. J., Costa, B., and Wedding, L. M. (2013). Lidar applications. *Coral reef remote sensing: A guide for mapping, monitoring and management*, pages 145–174.

[88] Richardson, D., Michel, P., Walsh, K., and Flynn, K. (2009). Numerical simulations of asteroids modelled as gravitational aggregates with cohesion. *Planetary and Space Science*, 57(2):183–192.

[89] Richardson, E. (1948). The impact of a solid on a liquid surface. *Proceedings of the Physical Society*, 61(4):352.

[90] Riedel, C., Michael, G., Kneissl, T., Orgel, C., Hiesinger, H., and van der Bogert, C. H. (2018). A new tool to account for crater obliteration effects in crater size-frequency distribution measurements. *Earth and Space Science*, 5(6):258–267.

[91] Rincón, M., Márquez, A., Herrera, R., Galland, O., Sánchez-Oro, J., Concha, D., and Montemayor, A. (2022). Monitoring volcanic and tectonic sandbox analogue models using the kinect v2 sensor. *Earth and Space Science*, 9(6):e2020EA001368.

[92] Robbins, S. J. and Hynek, B. M. (2012). A new global database of mars impact craters 1 km: 1. database creation, properties, and parameters. *Journal of Geophysical Research: Planets*, 117(E5).

[93] Roddy, D. J., Pepin, R. O., and Merrill, R. B. (1977). Impact and explosion cratering. planetary and terrestrial implications. proceedings of the symposium on planetary cratering mechanics, flagstaff, arizona, september 13-17, 1976. *Impact and Explosion Cratering: Planetary and Terrestrial Implications*.

[94] Rogers, J. G., Trevor, A. J., Nieto-Granda, C., and Christensen, H. I. (2011). Simultaneous localization and mapping with learned object recognition and semantic data association. In *2011 IEEE/RSJ International Conference on Intelligent Robots and Systems*, pages 1264–1270. IEEE.

[95] Rowley, P. J., Kokelaar, P., Menzies, M., and Waltham, D. (2011). Shear-derived mixing in dense granular flows. *Journal of Sedimentary Research*, 81(12):874–884.

[96] Ruiz-Suárez, J. (2013). Penetration of projectiles into granular targets. *Reports on Progress in Physics*, 76(6):066601.

[97] Salvi, J., Fernandez, S., Pribanic, T., and Llado, X. (2010). A state of the art in structured light patterns for surface profilometry. *Pattern recognition*, 43(8):2666–2680.

[98] Sarbolandi, H., Lefloch, D., and Kolb, A. (2015). Kinect range sensing: Structured-light versus time-of-flight kinect. *Computer vision and image understanding*, 139:1–20.

[99] Sauret, A. (2013). Smoothing out sandpiles: rotational bulldozing of granular material.

[100] Sauret, A., Balmforth, N., Caulfield, C., and McElwaine, J. (2014). Bulldozing of granular material. *Journal of fluid mechanics*, 748:143–174.

[101] Scheeres, D. J., Hartzell, C. M., Sánchez, P., and Swift, M. (2010). Scaling forces to asteroid surfaces: The role of cohesion. *Icarus*, 210(2):968–984.

[102] Sheward, D., Avdellidou, C., Cook, A., Sefton-Nash, E., Delbo, M., Cantarella, B., and Zanatta, L. (2022). Pynaple: Lunar surface impact crater detection. *Monthly Notices of the Royal Astronomical Society*, 514(3):4320–4328.

[103] Shoemaker, E. M. (1977). Why study impact craters. In *Impact and explosion cratering: Planetary and terrestrial implications*, pages 1–10.

[104] Stein, F., Medioni, G., et al. (1992). Structural indexing: Efficient 3-d object recognition. *IEEE Transactions on Pattern Analysis and Machine Intelligence*, 14(2):125–145.

[105] Su, X. and Chen, W. (2001). Fourier transform profilometry:: a review. *Optics and lasers in Engineering*, 35(5):263–284.

[106] Tortini, R., Bonali, F. L., Corazzato, C., Carn, S. A., and Tibaldi, A. (2014). An innovative application of the kinect in earth sciences: quantifying deformation in analogue modelling of volcanoes. *Terra Nova*, 26(4):273–281.

[107] Tsuda, Y., Yoshikawa, M., Saiki, T., Nakazawa, S., and Watanabe, S.-i. (2019). Hayabusa2–sample return and kinetic impact mission to near-earth asteroid ryugu. *Acta Astronautica*, 156:387–393.

[108] Turtle, E., Pierazzo, E., Collins, G., Osinski, G., Melosh, H., Morgan, J., and Reimold, W. (2005). Impact structures: What does crater diameter mean. *Large meteorite impacts III*, 384:1–24.

[109] Uehara, J., Ambroso, M., Ojha, R., and Durian, D. J. (2003). Low-speed impact craters in loose granular media. *Physical Review Letters*, 90(19):194301.

[110] Umbanhowar, P. and Goldman, D. I. (2010). Granular impact and the critical packing state. *Physical review E*, 82(1):010301.

[111] Van der Jeught, S. and Dirckx, J. J. (2016). Real-time structured light profilometry: a review. *Optics and Lasers in Engineering*, 87:18–31.

[112] Vera, L., Gimeno, J., Coma, I., and Fernández, M. (2011). Augmented mirror: interactive augmented reality system based on kinect. In *13th International Conference on Human-Computer Interaction (INTERACT)*, number Part IV, pages 483–486. Springer.

[113] Veverka, J., Thomas, P., Harch, A., Clark, B., Bell III, J., Carcich, B., Joseph, J., Chapman, C., Merline, W., Robinson, M., et al. (1997). Near's flyby of 253 mathilde: Images of a c asteroid. *Science*, 278(5346):2109–2114.

[Viera López, Gustavo and Corrales Machín, Frank] Viera López, Gustavo and Corrales Machín, Frank. Craterslab. https://github.com/gvieralopez/craterslab.

[115] Walsh, A. M., Holloway, K. E., Habdas, P., and de Bruyn, J. R. (2003). Morphology and scaling of impact craters in granular media. *Physical review letters*, 91(10):104301.

[116] Walsh, K. J., Richardson, D. C., and Michel, P. (2008). Rotational breakup as the origin of small binary asteroids. *Nature*, 454(7201):188–191.

[117] Wasenmüller, O. and Stricker, D. (2017). Comparison of kinect v1 and v2 depth images in terms of accuracy and precision. In *Computer Vision–ACCV 2016 Workshops: ACCV 2016 International Workshops, Taipei, Taiwan, November 20-24, 2016, Revised Selected Papers, Part II 13*, pages 34–45. Springer.

[118] Wegener, A. and Celâl Şengör, A. (1975). The origin of lunar craters. *The moon*, 14:211–236.

[119] Whittaker, E. (1949). Laplace. *The Mathematical Gazette*, 33(303):1–12.

[120] Wünnemann, K., Collins, G., and Melosh, H. (2006). A strain-based porosity model for use in hydrocode simulations of impacts and implications for transient crater growth in porous targets. *Icarus*, 180(2):514–527.

[121] Yang, L., Zhang, L., Dong, H., Alelaiwi, A., and El Saddik, A. (2015). Evaluating and improving the depth accuracy of kinect for windows v2. *IEEE Sensors Journal*, 15(8):4275–4285.

[122] Yeomans, D. K., Barriot, J.-P., Dunham, D., Farquhar, R., Giorgini, J., Helfrich, C., Konopliv, A., McAdams, J., Miller, J., Owen Jr, W., et al. (1997). Estimating the mass of asteroid 253 mathilde from tracking data during the near flyby. *Science*, 278(5346):2106–2109.

[123] Zhang, D. and Foda, M. (1997). An instability mechanism for the sliding motion of finite depth of bulk granular materials. *Acta mechanica*, 121(1-4):1–19.

[124] Zhang, S. and Yau, S.-T. (2009). High dynamic range scanning technique. *Optical Engineering*, 48(3):033604–033604.

[125] Zhang, Z. (2000). A flexible new technique for camera calibration. *IEEE Transactions on pattern analysis and machine intelligence*, 22(11):1330–1334.

[126] Zhou, F., Advani, S. G., and Wetzel, E. D. (2004). Slow drag in granular materials under high pressure. *Physical Review E*, 69(6):061306.

Appendix A

Supplementary Material

The supplementary material for visualization and analysis, along with a comprehensive description, can be found at the following link:
https://github.com/machinfc/supplemantary_material.git

The sequence of RGB and differential images, along with videos at 960 fps, illustrates the increased transfer of vertical to horizontal momentum as the impact surface becomes more compact in impacts from a free fall height of 20 meters onto loosely and compacted sandbox targets, as well as onto a solid surface.